bioRxiv preprint doi: https://doi.org/10.1101/772517; this version posted January 7, 2021. The copyright holder for this preprint (which was not certified by peer review) is the author/funder, who has granted bioRxiv a license to display the preprint in perpetuity. It is made available under aCC-BY-NC-ND 4.0 International license.

Descending neocortical output critical for skilled forelimb movements is distributed across projection cell classes

Junchol Park[1,†,*], James W. Phillips[1,2,†], Kathleen A. Martin[1,3], Adam W. Hantman[1], and Joshua T. Dudman[1,*]

[1] Janelia Research Campus, Howard Hughes Medical Institute, Ashburn, VA 20147
[2] Department of Physiology, Development and Neuroscience, University of Cambridge, UK
[3] *current address:* Center for Neural Science, New York University, New York, NY, USA
[*] *correspondence*: parkj@janelia.hhmi.org, dudmanj@janelia.hhmi.org
[†] *co-first authors*

Abstract

Motor cortex is a key node in the forebrain circuits that enable flexible control of limb movements. The influence of motor cortex on movement execution is primarily carried by either pyramidal tract neurons (PT), which project directly to the brainstem and spinal cord, or intratelencephalic neurons (IT), which project within the forebrain. The logic of the interplay between these cell types and their relative contribution to the coordination and scaling of forelimb movements remains unclear. Here we combine large-scale neural recordings across all layers of motor cortex with cell-type specific perturbations in a cortex-dependent mouse behavior: kinematically-variable manipulation of a joystick. Our data demonstrate that descending neocortical motor commands are distributed across projection cell classes. IT neuron activity, in comparison to PT neurons, carries a larger fraction of information about gross movement kinematics. We find that forelimb movements are robust to optogenetic silencing of PT output, but substantially impaired by silencing Layer 5a IT projection neurons. Dorsal striatum is the unique extracortical integration point for IT and PT output pathways and its activity was more dependent upon IT input than PT input during movement execution. These data indicate that forebrain extrapyramidal pathways can be critical for regulating kinematics of motor skills.

Introduction

Cortical control of movement in vertebrates stems from two major classes of output pathways that arise from pyramidal and intratelencephalic tract neurons [1]. Individual pyramidal tract (PT) neurons project directly to brainstem and spinal cord, along with many other descending systems [2–5]. The other major class of deep motor cortical output projection are the intratelencephalic (IT) or corticostriatal projection neurons of layer 5 and layer 2/3 [2,5–8]. The two major targets of the IT pathway are the cortex itself and the striatum of both hemispheres. Expansion and diversification of IT neuron populations appears to be a major contributor to changes in motor cortical cell types in the mammalian lineage [1].

bioRxiv preprint doi: https://doi.org/10.1101/772517; this version posted January 7, 2021. The copyright holder for this preprint (which was not certified by peer review) is the author/funder, who has granted bioRxiv a license to display the preprint in perpetuity. It is made available under aCC-BY-NC-ND 4.0 International license.

Due to their proximity to spinal motor neurons, PT neurons have generally been argued to be the primary source of descending forebrain motor commands [3,9–11]. However, many studies have observed substantial movement execution related activity in non-PT cell types in motor cortex [8,12–17]. While subcortical structures have generally been argued to contribute to multiple aspects of movement such as locomotion (reticular pathways that modulate central pattern generators [18]), or orienting and escape movements (modulation of descending circuits from tectum [19–21]). However, one prominent subcortical circuit, basal ganglia which is an afferent target of both IT and PT neurons, is known to be critical for controlling movement execution for skilled, dexterous forelimb movements [22–25] and is closely associated with regulation of vigor [26,27]. This implies a tight interplay of descending motor command signals across the IT and PT classes of projection neurons regulated by the complex microcircuitry of motor cortex[11]. However, the logic of the interplay between these cell types and their relative contribution to descending forebrain control of skilled forelimb movements remains unclear.

Why might the neocortex have two classes of output pathway? One possibility is that they contribute to different movement parameters employed to solve distinct control problems. For example, one may need to issue the same movements over a continuous range of vigor [28], utilize one or both forelimbs in a coordinated fashion [29], target the grasping of variable manipulanda [30], disinhibition or co-contraction of muscle groups [31], or reach out and grasp an object [32] with power or precision [16,17]. The circuit mechanisms that allow the same motor cortical circuits to control these diverse control demands have been difficult to understand [33]. Another possibility is that consistent dynamics [34] across the two systems can be flexibly configured to use varying combinations of pathways - a proposal that can allow robustness against perturbation of a given cell type [35]. To date, there is data to support both relatively circumscribed functions of individual projection neuron classes [9,36] and remarkable robustness to perturbation [37–40].

Here we sought to address this question by combining large-scale neural recording across the entire motor cortical depth and striatum with cell-type specific identification and perturbation in the context of mice performing a skilled forelimb motor task. This allowed us to explore the contribution of these two distinct cell classes to the control of forelimb movements. Cell-type specific perturbation during movement execution revealed that inactivation of IT output dramatically impaired vigorous forelimb movements. PT inactivation had a very modest effect on vigor, whilst a subtle but significant lateral

bioRxiv preprint doi: https://doi.org/10.1101/772517; this version posted January 7, 2021. The copyright holder for this preprint (which was not certified by peer review) is the author/funder, who has granted bioRxiv a license to display the preprint in perpetuity. It is made available under aCC-BY-NC-ND 4.0 International license.

deviation in the movement trajectory was observed. This indicates that IT pathways are a critical component of cortical motor commands in a cortex-dependent forelimb task. Cell-type specific perturbation and simultaneous recording of motor cortex and striatum revealed that inactivation of PT and IT populations had opposite effects on the striatal neural activity during movement that could partially account for the differential behavioral effects of the two projection cell classes. This provides a key insight into how the dynamics of the two major output pathway cell types in motor cortex are coordinated for flexible, robust control of forelimb movements.

Results

To assess how neocortical function is related to a flexible, skilled forelimb movement we used a task [23,24] in which mice were trained to make self-initiated (uncued) movements of varying amplitude to obtain a delayed (1 s) water reward. This task allowed us to isolate forelimb movements from reward collection and also examine changes in neural activity associated with a motor command variable - scaling of movement amplitude (9.35 ± 1.91 mm, range: 3.49−29.26 mm). Briefly, in the variable amplitude operant (VAO) task head-fixed mice had to move a joystick past a threshold of varying amplitude across three blocks to obtain a delayed water reward (Fig. 1a-b, Supplementary Video 1). After several weeks of training, mice were able to adjust reach amplitude across blocks to efficiently collect rewards (Fig. 1c, repeated measures ANOVA, $F_{2,16} = 13.28$, $p = 4.0\times10^{-4}$, pairwise test between blocks, $p < 0.05$; n=6 mice, 9 out of 11 total sessions, in which mice completed all three blocks were statistically analyzed).

We first asked whether activity in the forelimb motor cortex ($MCtx^{FL}$) was critical for performance of the VAO task by using optogenetic inactivation during movement execution. First, we allowed the initiation of movement to occur and then rapidly triggered [24] optical inactivation of $MCtx^{FL}$ using VGAT-ChR2 mouse [41]. As in other mouse forelimb operant tasks, *e.g.* joystick [42] or reach-to-grasp [32,43], we found that $MCtx^{FL}$ was critical for execution of a normal amplitude and speed movement (Fig. 1d-e, Supplementary Video 1; ANOVA, amplitude; $F_{1,10} = 11.33$, $p = 0.007$; speed; $F_{1,10} = 47.55$, $p = 4.22\times10^{-5}$). In addition, tonic inactivation of $MCtx^{FL}$ around the end of inter-trial intervals (ITI) (when reaches are most likely to commence) significantly reduced the probability of reach initiation (Fig. 1f, ANOVA, $F_{1,10} = 8.38$, $p = 0.016$). Finally, optogenetic activation of combined layer 5 $MCtx^{FL}$

bioRxiv preprint doi: https://doi.org/10.1101/772517; this version posted January 7, 2021. The copyright holder for this preprint (which was not certified by peer review) is the author/funder, who has granted bioRxiv a license to display the preprint in perpetuity. It is made available under aCC-BY-NC-ND 4.0 International license.

output pathways (using the Rbp4-cre mouse line [5]) was sufficient to invigorate movements (Extended Data Fig. 1). Thus, these data provide causal evidence that $MCtx^{FL}$ activity modulates the vigor with which forelimb movements are executed in mice, similar to stimulation of motor cortex in primates [44].

Movement-related neural activity is broadly distributed

To examine neural activity across all layers of $MCtx^{FL}$ during forelimb movements we used Neuropixels probes [45]. We recorded neuronal activity (224 ± 17 units per session, total 10 recording sessions) across all layers of forelimb motor cortex, dorsal and ventral striatum (Fig. 1g). A total of 2241 well-isolated and histologically-verified (see Methods) single units were recorded across $MCtx^{FL}$ (N=1102) and underlying striatum (STR, N=1139 units, Extended Data Figs. 2 & 3). Task-related activity was distributed across the entire recording depths including many single units in $MCtx^{FL}$ and dorsal STR (dSTR) with robust movement-timed activity (Fig. 1h-i, Extended Data Fig. 4a). The interval (1 s) between crossing of movement threshold and reward delivery revealed clear reward/consummatory period correlates in ventral striatum as expected, but also revealed a substantial number of units in $MCtx^{FL}$ primarily modulated around the time of reward collection (Fig. 1i, Extended Data Fig. 4a). Activity in a substantial fraction of $MCtx^{FL}$ units correlated with movement kinematics (Fig. 1h).

The activity of a population of neurons can be viewed as a trajectory in a high dimensional space where every moment in time in the trajectory reflects the instantaneous firing rate of each neuron in the population (Fig. 1j) [46]. The activity of $MCtx^{FL}$ or striatal neurons projected onto the first 3 principal components (PCs) reveals population trajectories that largely varied along one dimension during execution of forelimb movements and an orthogonal dimension during reward delivery and consumption (Extended Data Figs. 4b-d, 5a-c). This indicates that at least partially separable ensembles of neurons are active during forelimb movements and reward collection - made apparent due by the largely independent timing of forelimb movements and consumptive licking in the VAO task (Fig. 1b). To examine population activity related specifically to the kinematics of forelimb movements we used a targeted dimensionality reduction [47] with cross validation (see Methods). Using this method we found an axis along which the variance of neural

bioRxiv preprint doi: https://doi.org/10.1101/772517; this version posted January 7, 2021. The copyright holder for this preprint (which was not certified by peer review) is the author/funder, who has granted bioRxiv a license to display the preprint in perpetuity. It is made available under aCC-BY-NC-ND 4.0 International license.

activity was best explained by variance in forelimb movement kinematics (KN dimension; Fig. 1j). By projecting $MCtx^{FL}$ population activity onto the KN dimension we found that single trial, cross-validated population activity scaled with reach amplitude (Fig. 1k, Extended Data Fig. 6; ANOVA, $F_{2,27} = 31.82$, $p = 7.94 \times 10^{-8}$) indicating that $MCtx^{FL}$ neural activity in rodents is tuned to continuous kinematic parameters of movement execution analogous to many previous reports in primate MCtx [48].

Inhomogeneous laminar distribution of movement-timed activity in $MCtx^{FL}$

We next sought to examine how activity related to movement execution was distributed across the cell-types and output pathways of MCtx. Regressing trial by trial activity of individual units with the movement kinematics revealed significantly correlated units distributed relatively homogeneously throughout MCtx and dSTR (Fig. 1l). However, when we examined the time at which modulation of activity was maximal we found that peak timing of task-related activity was not distributed homogeneously (Fig. 1i, m, Extended Data Fig. 4a). For example, reward-timed activity was dominant in units recorded from ventral STR (Fig. 1i, Extended Data Fig. 4a). Within $MCtx^{FL}$ we observed a shift in the time of peak modulation of activity from movement-timed in superficial layers and upper layer 5 to around reward delivery in deeper layer 5 and layer 6 (Fig. 1i, m). This analysis suggests that the inhomogeneous distribution of peak timing of task-related activity could correspond to distinct projection cell classes. Specifically, the laminar pattern of IT neurons being distributed from the pia to upper layer 5, PT neurons primarily within deep layer 5, and corticothalamic neurons found in the layer 6 [5] suggests that movement-timed activity could be most prominent in IT-type neurons.

We found many units in superficial layer 5 with clear movement-timed modulation of activity. Simultaneously recorded neurons found in deeper layer 5 often exhibited strong modulation around the time of reward collection. This characteristic pattern of activity - positive modulation of activity around forelimb movement or negative modulation around forelimb movement and positive modulation around reward collection - was the dominant feature of population activity as revealed by examination of the leading PCs (total variance explained by first 3 PCs: $47 \pm 2.3\%$; Fig. 2b, Extended Data Fig. 4b-d). We describe these PCs as ‘move+’ and ‘move-’. We next examined how individual neurons contributed to each PC

bioRxiv preprint doi: https://doi.org/10.1101/772517; this version posted January 7, 2021. The copyright holder for this preprint (which was not certified by peer review) is the author/funder, who has granted bioRxiv a license to display the preprint in perpetuity. It is made available under aCC-BY-NC-ND 4.0 International license.

axis as a function of an estimate of its depth relative to the cortical surface (Fig. 2c). Consistent with the characterization of individual unit activity previously (Fig. 1m, 2a-c), the move+ and move- PCs had a distinct laminar distribution (Fig. 2d; two-way ANOVA, $F_{1,29}$ = 2.15, p = 4.0×10^{-4}, bin-by-bin test, $p < 0.05$). This indicates that $MCtx^{FL}$ population activity that tends to be less active during movement execution and increased during reward collection primarily arises around deep layer 5. In contrast, the large positive modulation of activity during forelimb movement execution that is correlated with kinematics primarily comes from more superficial layers.

Previous work has primarily focused on an analysis of differences in the mean activity per cell-type [9,12,36]. However, mean activity during movement could reflect a common modulation (*e.g.* movement initiation), as opposed to motor commands that are expected to correlate with kinematics [34]. The variable amplitude of forelimb movements in the joystick task provides rich trial by trial variation in kinematics with which to assess motor correlates. To assess whether the identified neural populations in our electrophysiological data were consistent with descending commands that instruct movement we trained decoders of movement amplitude (see Methods). An example of the performance of one such decoder for 20 concatenated forelimb movement epochs reveals that the amplitude and time course of movement could be captured across diverse kinematic profiles (Fig. 2e). Note that the decoder could accurately predict both the amplitude and direction (*e.g.* change in sign of X position) of movements. As with our analysis of population activity timing, we also found that the laminar distribution of units that contributed to movement decoding was inhomogeneous (Fig. 2f). We found that many units localized to layer 5 contributed to the decoding of movement kinematics consistent with the large enhancement of movement amplitude during activation of layer 5 projection neurons (Extended Data Fig. 1). However, as with previous analyses of peak timing of activity we again observed relatively little contribution of neurons in deep layer 5 (Fig. 2f). This decoding analysis thus suggests that the primary source of cortical motor commands may arise from cell-types localized to more superficial positions including upper layer 5.

Prevalence of motor command-like activity in IT neurons

bioRxiv preprint doi: https://doi.org/10.1101/772517; this version posted January 7, 2021. The copyright holder for this preprint (which was not certified by peer review) is the author/funder, who has granted bioRxiv a license to display the preprint in perpetuity. It is made available under aCC-BY-NC-ND 4.0 International license.

While distant laminar positions can reasonably be used to distinguish putative cell-class identity of recorded neurons (e.g. layer 3 vs layer 6), there is substantial overlap in laminar position for several critical cell types. Notably individual layer 5a IT and layer 5b PT neuron classes can be overlapping in their laminar positions [2,5,49]. Our optogenetic activation experiments indicated that these layer 5 pathways were sufficient to modulate forelimb movement kinematics, and decoding analysis suggested that units in layer 5 carry substantial information about movement kinematics. Thus, we next sought to use optogenetic tagging [9,50–52] to identify putative cell-type differences for the two major classes of projection cells in layer 5 - layer 5a IT and layer 5b PT neurons. While there is molecular diversity within these broad cell classes [1], mouse lines based upon Tlx3 and Sim1 [53] allow molecular access to the most complete supersets of layer 5 IT and PT types, respectively [5]. Here we use a robust and rapid optogenetic inhibitor [54] to identify neurons in awake animals to mitigate against confounds due to extensive cortical recurrent excitation [50].

To achieve labeling of PT neurons we used a retrograde virus (rAAV2-retro [55]) with conditional expression of the inhibitory opsin FLInChR [54] injected into the brainstem (pons) of Sim1-cre mice [53]. This strategy resulted in strong expression of an inhibitory opsin in brainstem-projecting PT neurons located within layer 5 of $MCtx^{FL}$ (Fig. 3a, Extended Data Fig. 2). A total of 111 units were identified as 'tagged' (PT^{+}). Importantly, tagging was performed after completion of the task but within the same recording session. In PT^{+} subset, activity was inhibited at short latency with half-maximal inhibition occurring within 17.48 ± 4.66 ms after illumination onset (Fig. 3a, c, f, Extended Data Fig. 7; see Methods for statistical criteria for tagging). To identify layer 5 IT neurons we used a similar retrograde labeling strategy with FLInChR injected into the dorsal striatum of Tlx3-cre [53,56] mice. This led to expression of FLInChR in striatum-projecting IT neurons within layer 5 of $MCtx^{FL}$ (Extended Data Fig. 2). A total of 30 units were identified as 'tagged' (IT^{+}) with half-maximal inhibition occurring within 26.83 ± 8.11 ms (Fig. 3b, c, h). Further consistent with selective identification of layer 5 PT and IT type neurons, the vast majority of optotagged units were distributed at depths consistent with layer 5 (Fig. 3c; depth estimates from Allen Reference Atlas).

We next compared activity of these two populations of putative, identified cell-types during task performance. Individual examples often revealed dramatic differences in the

bioRxiv preprint doi: https://doi.org/10.1101/772517; this version posted January 7, 2021. The copyright holder for this preprint (which was not certified by peer review) is the author/funder, who has granted bioRxiv a license to display the preprint in perpetuity. It is made available under aCC-BY-NC-ND 4.0 International license.

timing of activity across the two populations (Fig. 3d-e). The modulation of activity in PT^+ population was significantly weaker than the rest of the $MCtx^{FL}$ populations during forelimb movement (Fig. 3d, f, g, j; group x time interaction; repeated measures ANOVA, $F_{1,40} = 10.10$, $p = 4.66x10^{-61}$, main effect of group; ANOVA, $F_{1,572} = 21.54$, $p = 4.30x10^{-6}$). In contrast, IT^+ population displayed a significantly greater activity compared to PT^+ (Fig. 3e, h, i, j; group x time interaction; repeated measures ANOVA, $F_{1,40} = 7.78$, $p = 2.65x10^{-42}$, main effect of group; ANOVA, $F_{1,139} = 25.29$, $p = 1.49x10^{-6}$). Many PT^+ neurons exhibited suppressed activity around reach start (Fig. 3f, g, Extended Data Fig. 7). Moreover, positive modulation of activity, when apparent in a subset of PT^+ neurons, tended to be delayed relative to movement initiation (Fig. 3d, j, k-l). The activity of the majority of PT^+ neurons (69.4%) peaked after the reward delivery, while the majority of IT^+ neurons (80%) were most active prior to it (Fig. 3k; $\chi^2_1 = 23.77$, $p = 1.08x10^{-6}$). Likewise, the majority of PT^+ neurons showed the reward to reach activity ratio greater than 1 (64%), while the ratio was less than 1 for most IT^+ neurons (76.7%) (Fig. 3l; $\chi^2_1 = 15.77$, $p = 7.14x10^{-5}$).

Identifying cell-types via optogenetic tagging has been an important technique that has clarified cell-type specific basis of diverse neuronal correlates; however, it is also subject to well known limitations [9,50]. Thus, we sought to use a complementary method to assess the cell-type specific differences in the $MCtx^{FL}$ neural correlates of forelimb movements. We used cell-type specific calcium imaging to more precisely target two major layer 5 neuron populations in $MCtx^{FL}$. Specifically, we focused on superficial layer 5 IT neurons that provide dense corticostriatal projections [7,57] and are localized in a region that appeared to have reliable movement-timed activity in our task [8] (Figs. 1i, m, 2). We used a virally-driven expression of GCaMP6f in Sim1-cre and Tlx3-cre mice [9,53] which are known to preferentially drive expression of transgenes in deep layer 5b PT neurons and superficial layer 5a IT projection neurons, respectively (Fig. 4a-b; Sim1-cre: 8 mice, 19 imaging sessions, N=1576 ROIs. Tlx3-cre: 7 mice, 14 imaging sessions, N=1006 ROIs) [9,53,57,58].

Overall the average PT and IT activity showed prominent differences that were consistent with the electrophysiology data. IT neurons, similar to electrophysiologically recorded IT^+ neurons, showed greater peri-movement activation than PT neurons, while PT neurons had greater activation timed to reward collection and the intertrial interval activity (Fig. 4c-d). Analogous to the electrophysiological experiments we examined trajectories of

bioRxiv preprint doi: https://doi.org/10.1101/772517; this version posted January 7, 2021. The copyright holder for this preprint (which was not certified by peer review) is the author/funder, who has granted bioRxiv a license to display the preprint in perpetuity. It is made available under aCC-BY-NC-ND 4.0 International license.

population activity in a low dimensional state space spanned by the leading PCs. The first PC provided a dimension that distinguished activity of PT and IT populations. Cells with a negative loading on to the first PC (PC1−) were characterized by prominent activation around movement execution and were more likely to be IT neurons. In contrast, cells with a positive loading (PC1+) characterized by relatively suppressed activity during movement and more reward-timed modulation of activity were more likely to be PT neurons (Fig. 4e-g, PT/IT difference on PC1: $p < 5.35 \times 10^{-45}$, independent t-test).

Inactivation of Layer 5 IT neurons robustly decreases skilled forelimb movement amplitude

These data suggest a prevalence of motor command-like activity in IT neurons that are distributed throughout the cortical depth in $MCtx^{FL}$ [5]. Layer 5 PT neurons, by contrast, exhibited mixed activity and prominent activity around reward delivery. We next sought to directly assess the functional roles of these cell classes. As a means of cell-type specific perturbation, we used expression of a potent optogenetic inhibitor (FLInChR [54]) to inactivate IT or PT $MCtx^{FL}$ populations. Analogous to the labelling strategy for expression calcium indicators, we used a viral strategy with two mouse lines that label as broad a class as possible [5,53,57] layer 5 IT (Tlx-cre) and PT (Sim1-cre) neurons (Extended data Fig. 2).

To assess the relative contribution of these pathways to the execution of skilled forelimb movements we triggered laser delivery to the earliest time point of reach initiation [24] detected online for a random subset (~25%) of trials (Fig. 5a; also as in Fig. 1d-e). Suppression of activity in $MCtx^{FL}$ Layer 5 IT neurons had a large effect on movement kinematics (Fig. 5b-c, ANOVA, amplitude; $F_{1,12} = 16.83$, $p = 0.001$; speed; $F_{1,12} = 10.62$, $p = 0.007$) consistent with the prevalence of motor command-like activity observed in both electrophysiological and imaging datasets. In contrast, transient optogenetic suppression of PT neuron activity had a much smaller effect on the amplitude and speed of forelimb movements in the skilled joystick movement task (Fig. 5d-e, ANOVA, amplitude; $F_{1,10} = 3.80$, $p = 0.080$; speed; $F_{1,10} = 2.78$, $p = 0.127$) despite producing robust suppression of activity (Fig. 7b, Extended Data Fig. 9).

Cell-type and circuit specific performance of movement kinematic decoding

bioRxiv preprint doi: https://doi.org/10.1101/772517; this version posted January 7, 2021. The copyright holder for this preprint (which was not certified by peer review) is the author/funder, who has granted bioRxiv a license to display the preprint in perpetuity. It is made available under aCC-BY-NC-ND 4.0 International license.

The absence of a clear behavioral effect of acute layer 5 PT neuron inactivation is somewhat surprising, although it is well known that diverse species can compensate substantially for chronic loss of PT neurons [3]. However, a negative result may be accounted for by a number of possible explanations. One possibility is that given the prevalence of identified PT neurons with suppressed activity during movement, the further suppression via optogenetic inhibition could act to enhance movement. Indeed, it has been previously proposed that PT neurons may contribute to forelimb movements primarily via a "subcortical disinhibition" that may be a critical gate of motor commands [31]. Thus, we next examined whether the subset of PT neurons with suppressed activity during movement were consistent with activity that might shape movement kinematics during execution. If disinhibition is related to trial by trial changes in movement amplitude, then a population of PT^+ neurons with negative modulation of activity during movement and negative correlations with movement amplitude should be prominent in the subset of PT neurons with suppressed activity. However, we found little evidence for such a pattern (19% of PT^+ units in the lower left quadrant in Fig. 6a). Indeed, while PT^+ neurons with negative modulation during movement were apparent, they tended to have positive (Fig. 6a) and weaker (Fig. 6c, independent t-test, $t_{126}=3.65$, $p=3.82\times10^{-4}$) correlations with movement kinematics.

An additional possibility is that the PT neuron population as a whole does not contribute to descending motor commands and thus suppression of activity would not be expected to disrupt movement. To evaluate this possibility we examined the contribution of tagged PT neurons (regardless of sign of activity during movement) to the decoding performance (Fig. 2). This analysis revealed that PT^+ neurons in $MCtx^{FL}$ contributed a relatively small component to the explanatory power of the decoded, but significantly better than a shuffled decoder (Fig. 6d; rank sum test, $p<0.01$). This is consistent with the relative absence of large decoder weights in layer 5 (Fig. 2f). In contrast, we found that other population subsets exhibited superior decoding performance when compared with PT^+ neurons across all mice and sessions examined (Fig. 6d; rank sum test, all indicated $p<0.01$). Finally, we also trained a naive Bayes classifier to predict the tertile of movement amplitude from which a given trial was sampled. Cross-validation was used to train and test the classifier using non-overlapping trials and the same number of units sampled from each population subset. Again we found that the PT^+ population could be used to decode

bioRxiv preprint doi: https://doi.org/10.1101/772517; this version posted January 7, 2021. The copyright holder for this preprint (which was not certified by peer review) is the author/funder, who has granted bioRxiv a license to display the preprint in perpetuity. It is made available under aCC-BY-NC-ND 4.0 International license.

movement well above chance, albeit less than a matched number of IT^+ and other population subsets (Fig. 6e).

Inactivation of PT and IT neurons oppositely affect striatal activity

These decoding analyses indicate that activity of the PT population does indeed provide information about movement consistent with a partial contribution to descending motor commands. We found little support for a disinhibition mechanism to explain kinematic scaling. What then might account for the robustness of behavior during PT suppression? We consider several possible interpretations. First, one possibility is that the optogenetic suppression of PT neuron activity fails to produce a substantial perturbation during movement execution despite being sufficient to essentially completely inhibit activity in the absence of movement. Second, it is possible that the perturbation of Layer 5 IT neuron activity produced a much larger perturbation during behavior thereby accounting for the differential effects on behavior. Third, it is possible that inactivation of PT neurons causes less of an impairment of movement-related activity in downstream structures as compared to IT neuron output.

The striatum is unique in that it is the only forebrain, extra-cortical structure that integrates both IT and PT output [6,7]. Anatomical reconstructions of single neurons indicate that Layer 5 IT neurons provide much more dense axonal innervation of striatum (per neuron) as illustrated in the example populations of complete single neuron reconstructions from the PT and IT anatomical classes (Fig. 7a) [2]. Previous work has indicated that striatum plays a critical role in determining the scaling of movement kinematics in this task [23,24] and similar tasks in other species [20,27,59]. We observed robust movement-related activity distributed throughout the dorsal striatum (Fig. 1). Thus, we next examined the effect of PT inactivation during movement execution as well as its effects on the downstream target dorsal striatum.

We first compared PT^+ neuron population activity during control (unperturbed) movements to activity during movements paired with optogenetic inactivation. This analysis revealed a dramatic suppression of activity, much larger than the modest suppression of activity observed in the PT^+ population during control movements (Fig. 7b, Extended Data Fig. 9a-b; ANOVA, $F_{1,220}$=61.72, p=1.74x10^{-13}). In contrast, the same analysis during IT perturbation revealed, if anything, a significant but lesser extent of inactivation

bioRxiv preprint doi: https://doi.org/10.1101/772517; this version posted January 7, 2021. The copyright holder for this preprint (which was not certified by peer review) is the author/funder, who has granted bioRxiv a license to display the preprint in perpetuity. It is made available under aCC-BY-NC-ND 4.0 International license.

(Fig. 7c; ANOVA, Extended Data Fig. 9c-d; $F_{1,58}$=4.22, p<0.05). Thus, it does not appear to be the case that either inactivation during movement is ineffective in PT neurons nor that there is a weaker or more limited optogenetic inactivation of PT neurons relative to IT neurons.

We next examined how activity in striatum was affected by PT and IT inactivation. In contrast to the similar suppression of PT and IT neurons in both cases we found a clear dissociation in striatal activity. Optogenetic suppression of IT neuron activity during movement results in a corresponding decrease in striatal activity consistent with IT providing a strong source of excitatory input (Fig. 7d). However, during potent optogenetic silencing of PT neurons we found that striatal units on average increased activity during movement paired with PT inactivation (Fig. 7d, Extended Data Fig. 10; striatal modulation by PT vs IT inactivation; ANOVA, $F_{1,1146}$=35.49, p=3.41x10^{-9}). Striatum is composed of a number of cell types including both inhibitory projections neurons (MSNs) and local interneurons. Changes in MSN output are sufficient to alter forelimb movement kinematics [23]. Although it is not possible in these datasets to distinguish cell types based upon molecular identity, as with other brain regions these two broad classes are roughly distinguished by their baseline firing rate. PT inactivation resulted in clear increases in the activity in the subset of striatal units with low (<10 Hz) baseline firing rate consistent with an effect manifest in MSN projection neurons (Fig. 7e; ANOVA, $F_{1,978}$=31.46, p=2.65x10^{-8}).

The differential effect of PT and IT inactivation on striatal activity could partially account for the differential behavioral effects. One surprise was that a clear increase in MSN activity did not produce an increase in gross movement kinematics. It is possible that balanced changes in the opponent MSNs could produce little to no net effect on observed motor output [23,25]. However, we also wondered whether this could reflect a change in movement that we failed to detect when examining gross kinematics (Fig. 5; amplitude and speed). We next examined trajectories of individual forelimb movement in the presence and absence of PT inactivation. Indeed, such analyses revealed a small (~1.5 mm) change in the trajectories along the lateral axis that was time locked to PT inactivation and the increase in striatal activity (Fig. 7f; paired t-test, t_5=-7.26, p=7.73x10^{-4}). For comparison, we also examined the small subset of movement trajectories that were largely normal in the IT inactivation datasets ('breakthrough' movements). There was no reliable change in trajectory in this subset of behavioral trials (Fig. 7f; paired t-test, t_6=-1.88, p=0.11) providing some evidence that this effect was specific to PT inactivation.

bioRxiv preprint doi: https://doi.org/10.1101/772517; this version posted January 7, 2021. The copyright holder for this preprint (which was not certified by peer review) is the author/funder, who has granted bioRxiv a license to display the preprint in perpetuity. It is made available under aCC-BY-NC-ND 4.0 International license.

Finally, it has often been proposed or assumed that striatum likely receives movement execution-related information from MCtx via PT axon collaterals [8,26,27,59,60]. To better assess whether the increased average striatal responses might occlude a reduction in movement-related activity we first identified the KN dimension that reflected a significant change in the striatal population activity with movement amplitude (Fig. 7g, *left*; as done above for MCtx Fig. 1j-k; ANOVA, $F_{2,27} = 35.56$, $p = 2.72 \times 10^{-8}$). We then asked whether population activity along this dimension was altered by optogenetic inactivation of cortical input pathways. During PT inactivation there was no significant change in KN dimension activity (Fig. 7, *center*; paired t-test, $t_5=0.37$, $p=0.73$) consistent with a lack of effect on movement amplitude (Fig. 5d-e); by contrast, during IT inactivation there was a significant reduction in activity along the KN dimension (Fig. 7g, *right*; paired t-test, $t_3=-3.26$, $p<0.05$). Thus, although dorsal striatum carries substantial information about movement kinematics, PT inputs do not appear to be a major input source for such information.

Discussion

The central control of movement is characterized by the ability to execute movements adapted to achieve diverse goals with a common effector [61]. For example, animals can use their forelimbs over a continuously varying range of vigor [28], utilize one or both forelimbs in a coordinated fashion [29], targeted to variable manipulanda [30], or reach out to eccentric targets [32]. The circuit mechanisms that allow the same putative motor cortical circuits to control these movements has been difficult to understand [33]. Descending motor cortical output consists of two distinct projection classes - IT and PT. Much work has suggested that PT projection neurons are a critical source of descending motor control signals for dexterous and flexible limb movements [3,5]. There has been much less theorizing about the contribution of IT neuron output in the control of movement execution [17,20]. Here, we show that movement-related activity in the primary forelimb motor cortex is distributed across both output pathways in the context of a skilled forelimb movement. However, the distribution was not homogeneous - the IT projection class both contained activity that was more informative for decoding kinematics and behavior was much more sensitive to perturbation of IT neurons in layer 5 than PT neurons. This is surprising given the common assumption that pyramidal tract pathways are a primary or even sole determinant of flexible control of limb movements [10,36], but consistent with movement execution-related

bioRxiv preprint doi: https://doi.org/10.1101/772517; this version posted January 7, 2021. The copyright holder for this preprint (which was not certified by peer review) is the author/funder, who has granted bioRxiv a license to display the preprint in perpetuity. It is made available under aCC-BY-NC-ND 4.0 International license.

activity in diverse pyramidal neurons in rodents[11] and IT neuron populations in primates [8]. Our data are consistent with a central role for subcortical structures such as basal ganglia in the regulation of movement vigor [22,23] and critical functions for extrapyramidal motor pathways in regulating forelimb reaching movements [22,62–64].

Many studies of cortical encoding of movement have focused on cued movements of individual limbs along highly stereotyped trajectories[3]. Here we addressed the role of two major projection neuron subtypes in the motor cortex using a task that demands rescaling of movement amplitude. Although we attempted to produce a penetrant and robust inactivation of a broad class (Sim1+ [5,53,57]) of PT neurons, it is nearly impossible to rule out a small subset that is critically important, but failed to be targeted. We did observe a modest, but significant change in trajectory during PT inactivation that was dissociated from a change in the scaling of movement amplitude or speed. The notion that MCtx population activity can be substantially perturbed in ways that directly alter movement and those that are largely inconsequential for overt movement has been long standing. Indeed, this idea is central to account for preparatory activity in primary motor areas [65,66] and complex functional-tuning between individual neurons and the muscles they innervate [3,67]. One formulation of this idea is movement-potent vs movement-null dimensions of population activity [34,66,68,69]. However, to date it has been unknown how activity in defined cell-types relates to population activity broadly and to movement-potent dimensions specifically [70]. A common assumption is that PT output activity must be aligned with a movement-potent dimension [10,36,70]. However, tests of this point have been lacking because cell-type specific perturbations combined with physiological recordings have not been examined. Here we described cell-type specific perturbations of function that refine this notion indicating that IT neurons carry movement-potent activity that contributes substantially to determining scaling of movement amplitude. In contrast, our data suggest that movement-potent information related to trajectory is associated with the PT projection system, and PT inactivation has very little effect on amplitude and speed scaling. This may reflect the proposed role of the PT projection class for control of dexterous movement [3,5,16].

The dorsal striatum is the primary extra-cortical locus at which IT and PT neuron activity is integrated and thus provides unique insight into the coordination across these output pathways. The precise details of this integration to striatal activity remains unclear; however, there is substantial evidence that alterations in cell-type specific integration in striatum is responsible for multiple pathological states [6]. Here we describe the first cell-type

bioRxiv preprint doi: https://doi.org/10.1101/772517; this version posted January 7, 2021. The copyright holder for this preprint (which was not certified by peer review) is the author/funder, who has granted bioRxiv a license to display the preprint in perpetuity. It is made available under aCC-BY-NC-ND 4.0 International license.

specific perturbations of IT and PT activity together with simultaneous recording throughout all layers of MCtx and striatum as mice perform a skilled movement task. This led to a surprising dissociation in which IT inactivation produced a decrease in striatal activity as expected for a monosynaptic, excitatory input. PT inactivation, however, elicited a robust increase in activity in striatum. We find that an increase in striatal activity following PT inactivation is correlated with a change in trajectory heading time locked to the perturbation, although we cannot distinguish amongst a number of possible local[11] and long range circuit accounts of this phenotype. For example, an increase in the indirect pathway MSNs might be expected to reduce movement speed, whereas an increase in direct pathway MSN activity would be expected to increase movement speed [23]. Alternatively, if motor output is determined by the summation of PT output and basal ganglia output as proposed then the increase in striatal activity might be thought of as compensating for decreased PT output [26].

The discovery that direct motoneuron innervation by PT corticospinal neurons is unique to primates has provided an anatomical justification for accounts in which PT projections explain the remarkable dexterity of primate movements [3,16,17]. However, we also note that this is not the only evolutionary change characteristic of the primate motor cortex. Indeed, increasing diversity of IT neuron populations is also an innovation of primate motor cortex [1] and thus correlated with increasing refinement of motor skill. Our results strongly suggest that the coordination of distributed descending motor control signals across both major projection classes is critical in mice and may also be critical in other mammals. Our observation that descending motor commands are clearly present in IT neurons and then flow through dorsal striatum may help to explain the (relatively) modest effects of pyramidotomy to gross movement [38,71] and also help to explain how basal ganglia can be sufficient for movement execution following cortical lesions [72]. We note that basal ganglia output also plays a role in regulating the scaling of movement kinematics in primates [27,59,73,74]. The extent to which command-like motor cortical activity flows through IT output pathways in other motor tasks will continue to be a critical question for future experiments as well as further elucidating the specificity of motor control signals within diverse subtypes of these broad classes [5]. We suggest that such experiments will require simultaneous large-scale recording and perturbations that span identified cell-types and downstream integrative areas. Here we describe approaches that allow single trial decoding of variable movements and a direct assessment of the

bioRxiv preprint doi: https://doi.org/10.1101/772517; this version posted January 7, 2021. The copyright holder for this preprint (which was not certified by peer review) is the author/funder, who has granted bioRxiv a license to display the preprint in perpetuity. It is made available under aCC-BY-NC-ND 4.0 International license.

contribution of distinct projection classes. This approach will prove useful for increasingly precise refinement of our understanding of how dynamics distributed across distinct projection classes are coordinated for flexible and precise control of movement.

bioRxiv preprint doi: https://doi.org/10.1101/772517; this version posted January 7, 2021. The copyright holder for this preprint (which was not certified by peer review) is the author/funder, who has granted bioRxiv a license to display the preprint in perpetuity. It is made available under aCC-BY-NC-ND 4.0 International license.

REFERENCES

1. Bakken, T. E. *et al.* Evolution of cellular diversity in primary motor cortex of human, marmoset monkey, and mouse. *bioRxiv* 2020.03.31.016972 (2020) doi:10.1101/2020.03.31.016972.
2. Winnubst, J. *et al.* Reconstruction of 1,000 Projection Neurons Reveals New Cell Types and Organization of Long-Range Connectivity in the Mouse Brain. *Cell* (2019) doi:10.1016/j.cell.2019.07.042.
3. Lemon, R. N. Descending pathways in motor control. *Annu. Rev. Neurosci.* **31**, 195–218 (2008).
4. Kuypers, H. Anatomy of the Descending Pathways. in *Comprehensive Physiology* (ed. Terjung, R.) vol. 243 499 (John Wiley & Sons, Inc., 2011).
5. Muñoz-Castaneda, R., Zingg, B., Matho, K. S. & Wang, Q. Cellular Anatomy of the Mouse Primary Motor Cortex. *bioRxiv* (2020).
6. Shepherd, G. M. G. Corticostriatal connectivity and its role in disease. *Nat. Rev. Neurosci.* **14**, 278–291 (2013).
7. Dudman, J. T. & Gerfen, C. R. The basal ganglia. *The Rat Nervous System (Fourth Edition)* (2015).
8. Turner, R. S. & DeLong, M. R. Corticostriatal activity in primary motor cortex of the macaque. *J. Neurosci.* **20**, 7096–7108 (2000).
9. Li, N., Chen, T.-W., Guo, Z. V., Gerfen, C. R. & Svoboda, K. A motor cortex circuit for motor planning and movement. *Nature* **519**, 51–56 (2015).
10. Miri, A. *et al.* Behaviorally Selective Engagement of Short-Latency Effector Pathways by Motor Cortex. *Neuron* **95**, 683–696.e11 (2017).
11. Isomura, Y., Harukuni, R., Takekawa, T., Aizawa, H. & Fukai, T. Microcircuitry coordination of cortical motor information in self-initiation of voluntary movements. *Nat. Neurosci.* **12**, 1586–1593 (2009).
12. Peters, A. J., Chen, S. X. & Komiyama, T. Emergence of reproducible spatiotemporal activity during motor learning. *Nature* **510**, 263–267 (2014).
13. Chen, S. X., Kim, A. N., Peters, A. J. & Komiyama, T. Subtype-specific plasticity of inhibitory circuits in motor cortex during motor learning. *Nat. Neurosci.* **18**, 1109–1115 (2015).
14. Huber, D. *et al.* Multiple dynamic representations in the motor cortex during sensorimotor learning. *Nature* **484**, 473–478 (2012).
15. Peters, A. J., Lee, J., Hedrick, N. G., O'Neil, K. & Komiyama, T. Reorganization of corticospinal output during motor learning. *Nature Neuroscience* vol. 20 1133–1141 (2017).
16. Lemon, R. Recent advances in our understanding of the primate corticospinal system. *F1000Res.* **8**, (2019).
17. Isa, T., Kinoshita, M. & Nishimura, Y. Role of Direct vs. Indirect Pathways from the Motor Cortex to Spinal Motoneurons in the Control of Hand Dexterity. *Front. Neurol.* **4**, 191 (2013).
18. Kiehn, O. & Dougherty, K. Locomotion: Circuits and Physiology. *Neuroscience in the 21st Century* 1337–1365 (2016) doi:10.1007/978-1-4939-3474-4_42.
19. Branco, T. & Redgrave, P. The Neural Basis of Escape Behavior in Vertebrates. *Annu. Rev. Neurosci.* **43**, 417–439 (2020).
20. Park, J., Coddington, L. T. & Dudman, J. T. Basal Ganglia Circuits for Action Specification. *Annu. Rev. Neurosci.* (2020) doi:10.1146/annurev-neuro-070918-050452.
21. Swanson, L. W. Brain architecture: Understanding the basic plan. **263**, (2003).
22. Lemke, S. M., Ramanathan, D. S., Guo, L., Won, S. J. & Ganguly, K. Emergent modular neural control drives coordinated motor actions. *Nat. Neurosci.* (2019) doi:10.1038/s41593-019-0407-2.
23. Yttri, E. A. & Dudman, J. T. Opponent and bidirectional selection of movement parameters in the basal ganglia. *Nature* **533**, 402–406 (2016).
24. Panigrahi, B. *et al.* Dopamine Is Required for the Neural Representation and Control of Movement Vigor. *Cell* **162**, 1418–1430 (2015).
25. Cui, G. *et al.* Concurrent activation of striatal direct and indirect pathways during action initiation. *Nature* **494**, 238–242 (2013).
26. Yttri, E. A. & Dudman, J. T. A proposed circuit computation in basal ganglia: History-dependent gain. *Mov. Disord.* (2018).
27. Dudman, J. T. & Krakauer, J. W. The basal ganglia: from motor commands to the control of vigor. *Curr. Opin. Neurobiol.* **37**, 158–166 (2016).
28. Mazzoni, P., Hristova, A. & Krakauer, J. W. Why don't we move faster? Parkinson's disease, movement vigor, and implicit motivation. *J. Neurosci.* **27**, 7105–7116 (2007).
29. Tresilian, J. R. & Stelmach, G. E. Common organization for unimanual and bimanual reach-to-grasp tasks. *Exp. Brain Res.* **115**, 283–299 (1997).
30. Vargas-Irwin, C. E. *et al.* Decoding complete reach and grasp actions from local primary motor cortex populations. *J. Neurosci.* **30**, 9659–9669 (2010).
31. Ebbesen, C. L. & Brecht, M. Motor cortex - to act or not to act? *Nat. Rev. Neurosci.* **18**, 694–705 (2017).
32. Guo, J.-Z. *et al.* Cortex commands the performance of skilled movement. *Elife* **4**, e10774 (2015).
33. Shmuelof, L. & Krakauer, J. W. Are we ready for a natural history of motor learning? *Neuron* **72**, 469–476 (2011).

bioRxiv preprint doi: https://doi.org/10.1101/772517; this version posted January 7, 2021. The copyright holder for this preprint (which was not certified by peer review) is the author/funder, who has granted bioRxiv a license to display the preprint in perpetuity. It is made available under aCC-BY-NC-ND 4.0 International license.

34. Shenoy, K. V., Sahani, M. & Churchland, M. M. Cortical control of arm movements: a dynamical systems perspective. *Annu. Rev. Neurosci.* **36**, 337–359 (2013).
35. Barrett, D. G., Denève, S. & Machens, C. K. Optimal compensation for neuron loss. *Elife* **5**, (2016).
36. Economo, M. N. *et al.* Distinct descending motor cortex pathways and their roles in movement. *Nature* **563**, 79–84 (2018).
37. Kawai, R. *et al.* Motor cortex is required for learning but not for executing a motor skill. *Neuron* **86**, 800–812 (2015).
38. Lawrence, D. G. & Kuypers, H. G. The functional organization of the motor system in the monkey. I. The effects of bilateral pyramidal lesions. *Brain* **91**, 1–14 (1968).
39. Lawrence, D. G. & Kuypers, H. G. The functional organization of the motor system in the monkey. II. The effects of lesions of the descending brain-stem pathways. *Brain* **91**, 15–36 (1968).
40. Xu, J., Haith, A. M. & Krakauer, J. W. Motor Control of the Hand Before and After Stroke. *Clinical Systems Neuroscience* 271–289 (2015) doi:10.1007/978-4-431-55037-2_14.
41. Zhao, S. *et al.* Cell type–specific channelrhodopsin-2 transgenic mice for optogenetic dissection of neural circuitry function. *Nat. Methods* **8**, 745 (2011).
42. Bollu, T. *et al.* Automated home cage training of mice in a hold-still center-out reach task. *J. Neurophysiol.* **121**, 500–512 (2019).
43. Subramaniam, R., Kardon, B. M., Cohen, I. & Goldberg, J. H. Motor cortical inactivation reduces the gain of kinematic primitives in mice performing a hold-still center-out reach task. *BioRxiv* (2018).
44. Lemon, R. N., Johansson, R. S. & Westling, G. Corticospinal control during reach, grasp, and precision lift in man. *J. Neurosci.* **15**, 6145–6156 (1995).
45. Jun, J. J. *et al.* Fully integrated silicon probes for high-density recording of neural activity. *Nature* **551**, 232–236 (2017).
46. Cunningham, J. P. & Yu, B. M. Dimensionality reduction for large-scale neural recordings. *Nature Neuroscience* vol. 17 1500–1509 (2014).
47. Mante, V., Sussillo, D., Shenoy, K. V. & Newsome, W. T. Context-dependent computation by recurrent dynamics in prefrontal cortex. *Nature* **503**, 78–84 (2013).
48. Moran, D. W. & Schwartz, A. B. Motor cortical representation of speed and direction during reaching. *J. Neurophysiol.* **82**, 2676–2692 (1999).
49. Hooks, B. M. *et al.* Laminar analysis of excitatory local circuits in vibrissal motor and sensory cortical areas. *PLoS Biol.* **9**, e1000572 (2011).
50. Lima, S. Q., Hromádka, T., Znamenskiy, P. & Zador, A. M. PINP: a new method of tagging neuronal populations for identification during in vivo electrophysiological recording. *PLoS One* **4**, e6099 (2009).
51. Cohen, J. Y., Haesler, S., Vong, L., Lowell, B. B. & Uchida, N. Neuron-type-specific signals for reward and punishment in the ventral tegmental area. *Nature* **482**, 85–88 (2012).
52. Pan, W.-X., Brown, J. & Dudman, J. T. Neural signals of extinction in the inhibitory microcircuit of the ventral midbrain. *Nat. Neurosci.* **16**, 71–78 (2013).
53. Gerfen, C. R., Paletzki, R. & Heintz, N. GENSAT BAC cre-recombinase driver lines to study the functional organization of cerebral cortical and basal ganglia circuits. *Neuron* **80**, 1368–1383 (2013).
54. Brown, J. *et al.* Expanding the Optogenetics Toolkit by Topological Inversion of Rhodopsins. *Cell* **175**, 1131–1140.e11 (2018).
55. Tervo, D. G. R. *et al.* A Designer AAV Variant Permits Efficient Retrograde Access to Projection Neurons. *Neuron* **92**, 372–382 (2016).
56. Oh, S. W. *et al.* A mesoscale connectome of the mouse brain. *Nature* **508**, 207–214 (2014).
57. Hooks, B. M. *et al.* Topographic precision in sensory and motor corticostriatal projections varies across cell type and cortical area. *Nat. Commun.* **9**, 3549 (2018).
58. Chen, T.-W. *et al.* Ultrasensitive fluorescent proteins for imaging neuronal activity. *Nature* **499**, 295–300 (2013).
59. Turner, R. S. & Desmurget, M. Basal ganglia contributions to motor control: a vigorous tutor. *Curr. Opin. Neurobiol.* **20**, 704–716 (2010).
60. Januszewski, M., Schubert, P., Jain, V., Denk, W. & Fee, M. S. An anatomical substrate of credit assignment in reinforcement learning. *BioRxiv* (2020).
61. Krakauer, J. W., Hadjiosif, A. M., Xu, J., Wong, A. L. & Haith, A. M. Motor Learning. *Comprehensive Physiology* 613–663 (2019) doi:10.1002/cphy.c170043.
62. Esposito, M. S., Capelli, P. & Arber, S. Brainstem nucleus MdV mediates skilled forelimb motor tasks. *Nature* **508**, 351–356 (2014).
63. Alstermark, B. & Isa, T. Circuits for skilled reaching and grasping. *Annu. Rev. Neurosci.* **35**, 559–578 (2012).
64. Azim, E., Jiang, J., Alstermark, B. & Jessell, T. M. Skilled reaching relies on a V2a propriospinal internal copy circuit. *Nature* **508**, 357–363 (2014).
65. Churchland, M. M., Cunningham, J. P., Kaufman, M. T., Ryu, S. I. & Shenoy, K. V. Cortical preparatory activity: representation of movement or first cog in a dynamical machine? *Neuron* **68**, 387–400 (2010).

bioRxiv preprint doi: https://doi.org/10.1101/772517; this version posted January 7, 2021. The copyright holder for this preprint (which was not certified by peer review) is the author/funder, who has granted bioRxiv a license to display the preprint in perpetuity. It is made available under aCC-BY-NC-ND 4.0 International license.

66. Kaufman, M. T., Churchland, M. M., Ryu, S. I. & Shenoy, K. V. Cortical activity in the null space: permitting preparation without movement. *Nat. Neurosci.* **17**, 440–448 (2014).
67. Griffin, D. M., Hoffman, D. S. & Strick, P. L. Corticomotoneuronal cells are 'functionally tuned'. *Science* **350**, 667–670 (2015).
68. Li, N., Daie, K., Svoboda, K. & Druckmann, S. Robust neuronal dynamics in premotor cortex during motor planning. *Nature* **532**, 459–464 (2016).
69. Druckmann, S. & Chklovskii, D. B. Neuronal circuits underlying persistent representations despite time varying activity. *Curr. Biol.* **22**, 2095–2103 (2012).
70. Sussillo, D., Churchland, M. M., Kaufman, M. T. & Shenoy, K. V. A neural network that finds a naturalistic solution for the production of muscle activity. *Nat. Neurosci.* **18**, 1025–1033 (2015).
71. Alstermark, B. & Pettersson, L.-G. Skilled reaching and grasping in the rat: lacking effect of corticospinal lesion. *Front. Neurol.* **5**, 103 (2014).
72. Dhawale, A. K., Wolff, S. B. E., Ko, R. & Ölveczky, B. P. The basal ganglia can control learned motor sequences independently of motor cortex. *bioRxiv* 827261 (2019) doi:10.1101/827261.
73. Desmurget, M. & Turner, R. S. Motor sequences and the basal ganglia: kinematics, not habits. *Journal of Neuroscience* **30**, 7685–7690 (2010).
74. Turner, R. S., Desmurget, M., Grethe, J., Crutcher, M. D. & Grafton, S. T. Motor subcircuits mediating the control of movement extent and speed. *J. Neurophysiol.* **90**, 3958–3966 (2003).
75. Osborne, J. E. & Dudman, J. T. RIVETS: a mechanical system for in vivo and in vitro electrophysiology and imaging. *PLoS One* **9**, e89007 (2014).
76. Arenkiel, B. R. *et al.* In vivo light-induced activation of neural circuitry in transgenic mice expressing channelrhodopsin-2. *Neuron* **54**, 205–218 (2007).
77. Madisen, L. *et al.* A toolbox of Cre-dependent optogenetic transgenic mice for light-induced activation and silencing. *Nat. Neurosci.* **15**, 793–802 (2012).
78. Tennant, K. A. *et al.* The organization of the forelimb representation of the C57BL/6 mouse motor cortex as defined by intracortical microstimulation and cytoarchitecture. *Cereb. Cortex* **21**, 865–876 (2011).
79. Harrison, T. C., Ayling, O. G. S. & Murphy, T. H. Distinct cortical circuit mechanisms for complex forelimb movement and motor map topography. *Neuron* **74**, 397–409 (2012).
80. Goldey, G. J. *et al.* Removable cranial windows for long-term imaging in awake mice. *Nat. Protoc.* **9**, 2515–2538 (2014).
81. Podgorski, K. & Ranganathan, G. Brain heating induced by near-infrared lasers during multiphoton microscopy. *J. Neurophysiol.* **116**, 1012–1023 (2016).
82. Packer, A. M., Russell, L. E., Dalgleish, H. W. P. & Häusser, M. Simultaneous all-optical manipulation and recording of neural circuit activity with cellular resolution in vivo. *Nat. Methods* **12**, 140–146 (2015).
83. Theis, L. *et al.* Benchmarking Spike Rate Inference in Population Calcium Imaging. *Neuron* **90**, 471–482 (2016).
84. Kubota, S. I. *et al.* Whole-Body Profiling of Cancer Metastasis with Single-Cell Resolution. *Cell Rep.* **20**, 236–250 (2017).
85. Bogovic, J. A., Hanslovsky, P., Wong, A. & Saalfeld, S. Robust registration of calcium images by learned contrast synthesis. in *2016 IEEE 13th International Symposium on Biomedical Imaging (ISBI)* 1123–1126 (2016).
86. Liu, L. D., Chen, S., Economo, M. N., Li, N. & Svoboda, K. Accurate localization of linear probe electrodes across multiple brains. *bioRxiv* (2020).
87. Yu, B. M. *et al.* Gaussian-Process Factor Analysis for Low-Dimensional Single-Trial Analysis of Neural Population Activity. *Journal of Neurophysiology* vol. 102 614–635 (2009).
88. Churchland, M. M. *et al.* Neural population dynamics during reaching. *Nature* **487**, 51–56 (2012).
89. Tasic, B. *et al.* Shared and distinct transcriptomic cell types across neocortical areas. *Nature* **563**, 72–78 (2018).

bioRxiv preprint doi: https://doi.org/10.1101/772517; this version posted January 7, 2021. The copyright holder for this preprint (which was not certified by peer review) is the author/funder, who has granted bioRxiv a license to display the preprint in perpetuity. It is made available under aCC-BY-NC-ND 4.0 International license.

ACKNOWLEDGEMENTS

The authors thank Brett Mensh and Jason Keller for comments on earlier drafts of the manuscript. The authors thank several members of Janelia Research Campus for assistance with experimental hardware and software. For Neuropixels recordings Brian Barbarits, Jennifer Colonell, Tim Harris, James Jun, Bill Karsh, Wei-Lung Sun, and Eric Yttri provided critical assistance in developing the recording system and associated hardware. Dohoung Kim and Dave (Liu) Liu provided assistance for preparation and analysis of light sheet microscopy data from cleared mouse brains. For imaging experiments Dan Flickinger provided key assistance in the design of the microscope. Janelia Viral Tools and Vivarium provided critical support for these experiments. A.W.H. is a Group Leader and J.T.D. is a Senior Group Leader at Janelia Research Campus of the Howard Hughes Medical Institute (HHMI). This work was supported by funding from HHMI.

AUTHOR CONTRIBUTIONS

Conception and design of experiments J.W.P.,J.P.,A.W.H., & J.T.D. Analysis of electrophysiological data: J.P. & J.T.D. Data collection for behavioral experiments: J.P., J.W.P., K.A.M.; Data collection for electrophysiological experiments: J.P., J.G. Data collection for imaging experiments: J.W.P. The first draft of the paper was written by J.P. & J.T.D.; Final version was produced with input from all authors.

DATA AVAILABILITY

The data used in this manuscript will be made available at janelia.figshare.com upon publication or can be obtained via reasonable request to the authors at www.dudmanlab.org. Code for running all simulations in paper will be made available at https://github.com/DudLab and/or at http://dudmanlab.org upon publication.

bioRxiv preprint doi: https://doi.org/10.1101/772517; this version posted January 7, 2021. The copyright holder for this preprint (which was not certified by peer review) is the author/funder, who has granted bioRxiv a license to display the preprint in perpetuity. It is made available under aCC-BY-NC-ND 4.0 International license.

MATERIALS AND METHODS

Male and female mice, typically aged 8-16 weeks at time of surgery, were used in this study. All procedures were approved by the Janelia Research Campus Institutional Animal Care and Use Committee (IACUC) and were consistent with the standards of the Association for Assessment and Accreditation of Laboratory Animal Care. Mice were water restricted (1-1.2ml water/day), and their weight and signs of health were monitored daily as in[24].) Surgical methods closely followed those previously described[24,75] except where indicated below.

Behavior

The variable amplitude operant task was run as described previously [24] using a microcontroller based system (details can be obtained from http://dudmanlab.org/html/resources.html). After surgery (see below), mice were given 5 days of recovery prior to beginning water restriction (1ml water/day). Following 3-5 days of initial water restriction, they underwent 10-20 days training, which simply involved exposure to the task and self-learning. Mice were head-fixed in a custom made head restraint box using the RIVETS head-fixation apparatus [75]. The mouse's front paws rested on a metal bar attached to a spring-loaded joystick, which had unconstrained 2D maneuverability in the horizontal plane. Mice were trained to maneuver the joystick to certain thresholds varying across three different blocks (e.g. 4.2-5.7-4.2 mm) to obtain a sweetened water reward delivered 1 s after each threshold crossing. Rewards were followed by a 3 s inter-trial interval (ITI) in which no movements would be rewarded. There were up to 150 trials (50 trials per block) in electrophysiology and 120 trials per session in imaging (some sessions were incomplete), with one water reward being available per trial. All behavioral events (forelimb movements, licks) were recorded on separate channels at 25 kHz (USB-6366; National Instruments, Austin, Texas) then downsampled offline at 1 kHz. Forelimb movements were assessed offline to detect individual reaches based on the speed joystick movement. Time points of reach start and stop were defined as well as other kinematic properties such as duration, maximum amplitude and speed for each reach.

Extracellular electrophysiological identification and recording of PT and IT neurons in awake head-fixed mice

For cell-type specific in vivo recordings from motor cortex and striatum in mice performing the variable amplitude operant task, rAAV2-retro-CAG-Flex-FLInChR-mVenus (3.0E+12 GC/ml) was injected to the pons bilaterally (relative to lambda: 0.4 mm anterior, 0.4 mm lateral, 5.5, 5.75, 6 mm deep, 70 nL/depth) in Sim1-cre (KJ18Gsat RRID:MMRRC_037650-UCD) mice, selectively labeling a pyramidal type (PT) layer 5 population [36,53,55]. The same viral vector was injected to the dorsal striatum (relative to bregma: 0.5 mm anterior, 1.6 mm lateral, 2, 2.7, 3.5 mm deep) and cortex (site 1 : 0.9 anterior, 1.5 lateral, site 2: 0.1 anterior, 1.9 lateral, site 3: 0.1 anterior, 1.1 lateral, each site at 0.3 and 0.6 mm deep, 80nl/depth) in Tlx3-cre (PL56Gsat RRID:MMRRC_041158-UCD [53]) mice, selectively labeling a layer 5 IT population. Prior to recordings, a craniotomy was made over the recording sites (relative to bregra: 0.5 mm anterior, ±1.7mm lateral) at least 12 hours prior to recording under isoflurane anaesthesia. Exposed brain tissue was kept moist with phosphate-buffered saline at all times, and craniotomy sites were covered with Kwik-Sil elastomer (WPI) outside of the recording session.

For neural population recording using the Neuropixels probe [45], awake mice fully recovered from craniotomy were head-fixed in a RIVETS chamber [75]. A Neuropixels probe (option 3 phase A) with 374 recording sites was briefly (~2 minutes) dipped into the dil cell-labeling solution (ThermoFisher) to visualize probe tracks, then lowered through the craniotomy manually. After a slow, smooth descent (0.2 mm/min), the probe sat still at the target depth for at least 5 min before initiation of recording to allow the electrodes to settle. An Ag wire was soldered onto the reference pad of the probe and shorted to ground. This reference wire was connected to an Ag/AgCl wire was positioned on the skull. The craniotomy and the Ag/AgCl wire were covered with a saline bath. Voltage signals are filtered (high-pass above 300 Hz), amplified (200x gain), multiplexed and digitized (30 kHz) on the base, allowing the direct transmission of noise-free digital data from the probe, and were recorded using an open-source software SpikeGLX (https://github.com/billkarsh/SpikeGLX). Recorded data were pre-processed using an open-source software JRCLUST (https://github.com/JaneliaSciComp/JRCLUST) to identify single- or multi units in the primary motor

bioRxiv preprint doi: https://doi.org/10.1101/772517; this version posted January 7, 2021. The copyright holder for this preprint (which was not certified by peer review) is the author/funder, who has granted bioRxiv a license to display the preprint in perpetuity. It is made available under aCC-BY-NC-ND 4.0 International license.

cortex (M1) and STR. To assay FLInChR expression and responses, a fiber (200 mm core, 0.39 NA, Thorlabs) coupled to a 574 nm laser source (Omicron) was placed to deliver light onto the craniotomy. Single laser pulses of 1 s duration with power measured at the tip of the fiber of 4-8 mW were delivered 60 times with 8 s intervals. Mice were at rest after task completion during tagging.

For cell-type specific recordings from motor cortex in mice performing the reach-to-grasp task, rAAV2-retro-hSyn-GtACR2-KV-eGFP (8.5E+13 GC/ml) was injected to the pons bilaterally (relative to lambda: 0.4 mm anterior, 0.4 mm lateral, 5.5, 5.75, 6 mm deep, 30 nL/depth) in Sim1-cre (KJ18Gsat) mice, selectively labeling a pyramidal type (PT) layer 5 population. The same viral vector was injected to the dorsal striatum (relative to bregma: 0.5 mm anterior, 1.7 mm lateral, 2.8, 2.6, 2.4 mm deep) and cortex (0.5 mm anterior, 1.7 mm lateral, 1.0, 0.5 mm deep) in the right hemisphere of Slc17a7-cre mice to selectively label a layer 5 IT population in the left hemisphere. All recordings and optical silencing were conducted in the left hemisphere contralateral to the reaching hand (right).

A unit with a significant reduction in the spike count during the laser (paired t-test, α=0.01 and/or at least 60 % reduction relative to the baseline period) was considered to be optogenetically tagged.

Cell-type specific closed-loop perturbation of M1 neuronal activity

To examine the cell-type specific role of the deep layer 5 PT neurons in MCtx, we injected rAAV2-retro-CAG-Flex-FLInChR-mVenus[54,55] into the pons (relative to lambda: 0.4 mm anterior, 0.4 mm lateral, 5.5, 5.75, 6 mm deep, 70 nL/depth) in three Sim1-cre (KJ18Gsat [53]) mice. Viruses obtained from Janelia Viral Tools (https://www.janelia.org/support-team/viral-tools). To examine the role of the IT neurons in MCtx, we bilaterally injected the same virus into the dorsal striatum (relative to bregma: 0.5 mm anterior, 1.6 mm lateral, 2, 2.7, 3.5 mm deep, 150 nL/depth) and cortex (site 1 : 0.9 anterior, 1.5 lateral, site 2: 0.1 anterior, 1.9 lateral, site 3: 0.1 anterior, 1.1 lateral, each site at 300+600 microns deep, 80nl/depth) in five Tlx3-cre (PL56Gsat [53]), respectively. In closed-loop experiments, a 500 ms single pulse of 574 nm laser was delivered bilaterally in randomly selected 30 % of the trials immediately when mice moved the joystick by 1.5mm from the zero point taken at the end of each ITI.

To examine the general role of MCtx in control of forelimb movement regardless of the projection neuronal cell-type, we implanted optical fibers (200 mm core, 0.39 NA, Thorlabs) bilaterally to place fiber tips right onto the pia of the brain in VGAT-ChR2-eYFP [76] (Fig. 1d-f) or Rbp4-cre RRID:MMRRC_037128-UCD [53]::Ai32 RRID:IMSR_JAX:024109[77] (Extended Data Fig. 1) mice. In closed-loop experiments, a 500 ms single pulse of 473 nm laser was delivered in randomly selected trials triggered by a slight joystick movement caused by mice. In open-loop experiments, a 3 s single pulse of 473 nm laser was delivered in randomly selected 30 % of trials at a given time point (2 s after previous reward delivery during inter-trial interval in select trials) regardless of animals' behavior.

Cell-type specific two-photon calcium imaging

Viruses were AAV 2/1-Flex-GCaMP6f, diluted to $2*10^{12}$gc/ml [58] RRID:Addgene_58514 and obtained from Janelia Viral Tools (https://www.janelia.org/support-team/viral-tools). 5 injections performed in a cross-shape, centered on 1.6 lateral, 0.6 rostral. 20nL was ejected at 600um depth. This center was chosen based upon previous microstimulation work[78,79]. Imaging was restricted to one month after injection to minimise overexpression.

3mm-wide circular imaging windows were made over the left cortical hemisphere in all animals, following the method of Goldey *et al* [80]. Window implants were centered on the virus injection center, and fixed in place using cyanoacrylate glue and dental acrylic. Windows (custom ordered from Potomac photonics) were made by placing three windows together, with the top window being 3.5mm, the bottom two being 3mm, such that the top window rested on thinned skull area. This triple window arrangement was used to increase downward pressure on the brain and stabilize the brain motion.

Imaging was performed with a custom built two photon laser scanning microscope running scanImage software (latest versions, from 2013-2016; https://vidriotechnologies.com). GCaMP6f was excited with a ti:sapphire laser, tuned to 920nm. Imaging was typically performed at 33Hz via

bioRxiv preprint doi: https://doi.org/10.1101/772517; this version posted January 7, 2021. The copyright holder for this preprint (which was not certified by peer review) is the author/funder, who has granted bioRxiv a license to display the preprint in perpetuity. It is made available under aCC-BY-NC-ND 4.0 International license.

bidirectional scanning with a resonant galvo. Power at sample did not exceed 150mW. In poorer quality windows, frame rate was halved to allow an increase in peak pulse power. This was done to minimise photodamage from thermal effects [81]. Depth of recording ranged from 350um-450um, depending upon imaging clarity, corresponding to the proximal dendritic region of the apical dendrite.

All imaging data analysis was performed in Python using custom-written scripts unless otherwise stated. Imaging data was motion corrected in two stages. Firstly, an image average was taken for a session across all frames. Secondly, each frame was then motion registered to that image, based upon a Fourier-based cross-correlation approach to detect the optimal corrective displacement. The average was then re-taken, and the process repeated 3 times. The result of this image registration process was examined by eye for each session to check for errors.

Region of interest (ROI) extraction was done manually in imageJ software. ROIs with high baseline fluorescence, a putative marker for unhealthy cells, were not used[82]. Fluorescence traces were deconvolved to inferred rates using published code[83]. We note that this is not an attempt to claim specific firing rates of neurons, but rather to reduce the distorting effect of the calcium sensors' slow kinetics on the inferred activity. We did not attempt to calibrate these inferred spike rates with real rates.

Histology

Fluorescence light sheet microscopy of cleared mouse brain

At completion of all electrophygiological experiments, mice were perfused with 40 ml of cold PBS (pH 7.4) containing 20 U/ml heparin at ~10ml/min, and fixed with cold 4% PFA. Extracted brains were further fixed for 24hrs in 4% PFA. Fixed brains were delipidated using the CUBIC-L cocktail 10 w%/10w% N-butyldiethanolamine/Triton X-100 for a week. Delipidated brains underwent nuclear counterstaining with TO-PRO-3 (ThermoFisher) for a day. We then transparentized the delipidated brains in the refractive index (RI) matching cocktail CUBIC-R composed of 45 w%/30 w% antipyrine/nicotinamide for two days[84]. Finally, cleared brains were imaged using fluorescence light sheet microscopy (Zeiss Lightsheet Z.1) to visualize expression of FLInChR (509 nm), probe tracks (570 nm), and nuclear counterstaining (661 nm).

The imaged 3D brain volumes (v3D) were aligned to a standardized brain coordinate system (Allen Anatomical Template, AAT) using a semi-manual landmark-based method (big warp)[85]. The v3Ds were additionally aligned to the template MRI image volume (MRI3D) acquired using fixed brains in the skull to further correct for any distortion due to extraction of the brain from the skull [86]. Each probe track was manually marked on v3D fused with AAT, and the 3D coordinates of all electrode sites were finally determined on MRI3D using the mapping between AAT and MRI3D combined with the geometry of the Neuropixels probe. Using the 3D coordinates, each electrode site was labeled as a brain region according to AAT segmented into brain regions (Allen Reference Atlas, ARA). All cortical cells in our analyses were recorded from electrode sites verified to be in a motor cortical region. All cells recorded from electrodes located at the pial depth of 1.75 mm or upper (estimated by the manipulator) were assigned a motor cortical region. This depth of 1.75 mm agreed with our physiological estimation of the cortical border (Extended Data Fig. 3), thus, we considered 1.75 mm as the putative cortical border.

DATA ANALYSIS METHODS

Neural data analysis

Single unit data analyses and statistical tests were performed using custom-written codes in Matlab. Spikes of isolated single units in M1 and striatal areas were counted within 1-ms bins to generate the trial-by-bin spike count matrix per unit aligned to reach start or reward delivery. The trial-averaged firing rates were calculated within 50-ms bins and z-score normalized using the mean and standard deviation of its baseline (a 2500-ms period before reach start) firing rate.

Dimensionality reduction (PCA)

To find the direction along which the neural population activity most covaried during task performance and extract low dimensional neural population trajectories along these directions, PCA

bioRxiv preprint doi: https://doi.org/10.1101/772517; this version posted January 7, 2021. The copyright holder for this preprint (which was not certified by peer review) is the author/funder, who has granted bioRxiv a license to display the preprint in perpetuity. It is made available under aCC-BY-NC-ND 4.0 International license.

was performed on a data matrix D of size (b × t, n), where b and t are the number of 50-ms time bins and the number of trials, respectively, n is the number of neurons. The trial-by-trial binned spike counts are square-root transformed to construct D[87]. Applying PCA to D obtain X and W such that X = DW, where X is the projection of the data onto the principal components (PCs), which are orthonormal columns comprising W that contains the weights from neurons to PCs. To reveal the time-evolving patterns of population activity, $D_{t,b}$ were projected onto top three PCs, trial-averaged and strung together across time to generate neural population trajectories on each PC dimension versus time (Fig. 2b, Extended Data Figs. 4 & 5).

Targeted dimensionality reduction

To quantify representation of reach amplitude by the MCtx neural population we used a targeted dimensionality reduction [47] method. The goal was to identify the dimension (axis) within the state space of length N_{unit} defined by the activity of each unit, which account for neural response variance related to movement kinematic variables such as reach amplitude, speed, and the number of licking.

The analysis comprised three steps. First, we conducted PCA to denoise the population responses and focus our analyses on the subspace spanned by the first ten PCs [87,88]. A data matrix X of size (c × t, n) comprised averaged population responses corresponding to tertiles of three relevant movement kinematic variables - reach amplitude, speed, and lick count, where c and t were all possible 27 combinations of the three movement kinematic variable tertiles and the number of 50-ms time bins, respectively, n was the number of neurons. The PCs of this data matrix are vectors ν_a of length N_{unit}, and the denoising matrix D was built using the first ten PCs, where $D = \sum_{a=1}^{10} \nu_a \nu_a^T$ (see the denoised regression vectors defined below).

We used a multiple linear regression to quantify how much the activity of each unit varied as a function of movement kinematic variables:

$$r_{i,t}(k) = \beta_{i,t}(1)amplitude(k) + \beta_{i,t}(2)speed(k) + \beta_{i,t}(3)lick(k) + \beta_{i,t}(4),\ (eq.\ 1),$$

where $r_{i,t}(k)$ is the z-scored response of unit i at time t on trial k, $amplitude(k)$, $speed(k)$, $lick(k)$ are the maximum reach amplitude, reach speed, and the number of licking on trial k discretized as tertiles of all trials in each behavioral session, e.g. for $amplitude(k)$, 1, 2, 3 were assigned to trials of low, medium, high reach amplitudes. The last regression coefficient captures variance that is independent of the movement kinematic variables. The regression coefficients $\beta_{i,t}(\nu)$ indicate how much the trial-by-trial firing rate of unit i at a given time t during the trial, can be regressed onto each movement kinematic variable ν. To estimate the regression coefficients $\beta_{i,t}(\nu)$, a design matrix F_i of size $N_{coef} \times N_{trial}$ comprising values for each movement kinematic regressor across trials was built for each recorded unit i. The regression coefficients were then estimated as:

$$\beta_{i,t} = (F_i F_i^T)^{-1} F_i r_{i,t}.$$

We use the regression coefficients $\beta_{i,t}$ estimated for individual units to identify dimensions within state space along which the neural population activity most covaried with movement kinematic variables. For each task variable, a 'regression vector' $\beta_{\nu,t}$ of length N_{unit} is obtained whose entries $\beta_{\nu,t}(i)$ correspond to regression coefficients for kinematic variable ν, time t, and unit i. Regression coefficient vectors $\beta_{\nu,t}(i)$ are then denoised by projecting them into the subspace spanned by the first ten PCs using the denoising matrix D defined above:

$$\beta_{v,t}^{pca} = D\beta_{v,t},$$

Time-independent denoised regression vectors β_v^{max} are then obtained by identifying the time at which the denoised regression vectors have maximum norm.

$$\beta_v^{max} = \beta_{v,t_v^{max}}^{pca} \text{ with}$$

$$t_v^{max} = argmax_t \left\| \beta_{v,t}^{pca} \right\|,$$

Finally, we obtain orthogonal axes in state space corresponding to neural variance associated with movement kinematic variables by orthogonalizing β_v^{max} with QR decomposition:

bioRxiv preprint doi: https://doi.org/10.1101/772517; this version posted January 7, 2021. The copyright holder for this preprint (which was not certified by peer review) is the author/funder, who has granted bioRxiv a license to display the preprint in perpetuity. It is made available under aCC-BY-NC-ND 4.0 International license.

$$B^{max} = QR,$$

where $B^{max} = [\beta^{max}_{amplitude}\ \beta^{max}_{speed}\ \beta^{max}_{lick}]$ is a matrix whose columns are the time-independent denoised regression vectors β^{max}_{v}. The first three columns of Q correspond to the orthogonalized regression vectors $\beta^{\perp}_{v}$ which we refer to as the movement kinematic axes, $KN^{dim.}$, R^{speed}, and R^{lick} of length N_{unit}. Projection onto these axes reveal neural population activity as a function of movement kinematics (Fig.s 1g-h, 6g-j).

To focus on the neural population variance as a function of reach amplitude avoiding the issue of multicollinearity between movement kinematic variables in the linear regression model, we repeated targeted dimensionality reduction with only replacing *eq. 1* with *eq. 2* below with the rest of the analysis kept identical:

$$r_{i,t}(k) = \beta_{i,t}(1)amplitude(k) + \beta_{i,t}(2),\ (eq.\ 2).$$

Targeted dimensionality reduction using the two regression models identified almost identical axes as $KN^{dimension}$, and thus the projection scores appeared to be similar. Figures represent the result using *eq. 2*.

Two-fold cross-validation was used; i.e., data from half of randomly selected trials were used to define $KN^{dimension}$, and the data of the held out trials were projected to the $KN^{dimension}$. Consistent trajectories were observed across many iterations (Extended Data Fig. 6), indicating that there existed a stable dimension that captures covariance of neural population activity as a function of forelimb movement kinematics.

Linear (consensus) decoder

To assess the contribution of distinct neural populations to forelimb movement, we used a linear decoder to estimate the joystick movement based on the neural activity. The decoded estimates were then correlated with the actual joystick trajectories. The decoder defines linear mapping (W_{decode}) between the neural population activity and the two dimensional position of the joystick:

$$K = F^T \cdot W_{decode}$$

where F is the data matrix comprising the population vector of spike counts with the dimension of the number of units concatenated across all time bins and trials in the training data set. The matrix K comprises two vectors each corresponding to the estimated X and Y amplitudes of the joystick movement. We solve for W_{decode} as $W_{decode} = (F^T F)^{-1} F^T K$. For cross validation, we trained and tested the decoder using non-overlapping sets of data, i.e., different trials.

Naive Bayes classifier

To assess how informative distinct neural populations are of the executed movement amplitude, we used a Poisson naive Bayes classifier to decode which movement amplitude tertile (C_k, k=1,2,3) a given trial is sampled from. For each of 1000 iterations, data from each subpopulation (e.g. PT^+, IT^{put}, Striatum etc.) resampled to match the number of neurons per subpopulation are randomly split into 10 folds of trials. A Poisson likelihood function is given by the following:

$$P(\overline{x_t} \mid c_k) = \prod_{i=1}^{D} \frac{\lambda_{k_{i,t}}^{x_{i,t}} e^{-\lambda_{k_{i,t}}}}{x_{i,t}!},$$

where $\overline{x_t}$ is a population vector of spike counts at t^{th} time bin of a trial, k indicates a movement amplitude tertile. i indicates neuron label, 1 to D. $\lambda_{k_{i,t}}$ is the parameter for the Poisson distribution estimated using the 9 of the 10 folds by the following:

$$\lambda_{k_{i,t}} = \frac{1}{N_k} \sum_{n \in C_k} x_{n_{i,t}}$$

The posterior probability of a movement amplitude tertile given the spike count vector is provided by Bayes' theorem as follows:

$$P(c_k \mid \overline{x_t}) = \frac{P(\overline{x_t} \mid c_k) P(c_k)}{P(\overline{x_t})}$$

An estimated movement amplitude tertile is assigned to a given trial as follows:

bioRxiv preprint doi: https://doi.org/10.1101/772517; this version posted January 7, 2021. The copyright holder for this preprint (which was not certified by peer review) is the author/funder, who has granted bioRxiv a license to display the preprint in perpetuity. It is made available under aCC-BY-NC-ND 4.0 International license.

$$\widehat{c_k} = argmax_k P(\overline{x_t} \mid c_k)$$

The result of naive Bayes classifier analysis is quantified as the percentage of correctly estimated test folds.

bioRxiv preprint doi: https://doi.org/10.1101/772517; this version posted January 7, 2021. The copyright holder for this preprint (which was not certified by peer review) is the author/funder, who has granted bioRxiv a license to display the preprint in perpetuity. It is made available under aCC-BY-NC-ND 4.0 International license.

Supplemental videos:

Supplementary video 1. Example trials with/without closed-loop inactivation of MCtx^{FL} neural activity by activation of inhibitory neurons in VGAT-ChR2 mice.
(Left) A representative trial with closed-loop inactivation of MCtx^{FL}. A filled circle in the upper left corner indicates frames with laser on. Numbers in the bottom left corner indicate time relative to the laser onset triggered by slight movement of the animal. Video replay is at x0.2 speed.
(Right) A representative trial without closed-loop inactivation. An empty circle in the upper left corner indicates frames for which laser would have been delivered. Numbers in the bottom left corner indicate time relative to the pseudo laser onset.
Video 1 can be found online at:
https://www.dropbox.com/s/vy6dzrqwm4w1eix/Trial%2354_139_stim-Pstim%20%28Converted%29.mov?dl=0

bioRxiv preprint doi: https://doi.org/10.1101/772517; this version posted January 7, 2021. The copyright holder for this preprint (which was not certified by peer review) is the author/funder, who has granted bioRxiv a license to display the preprint in perpetuity. It is made available under aCC-BY-NC-ND 4.0 International license.

Figure legends

Figure 1. Distributed task related neural dynamics in a self-initiated variable amplitude operant task

a, Mice were trained to perform an self-initiated (uncued) variable amplitude operant task, in which movements were made for delayed reward. To perform this task, mice were head-fixed, and moved a joystick bimanually. **b**, *Top*, A representative trace of reach amplitude (i.e., distance from the 'zero' position reset at the end of each inter-trial interval) superimposed with the rasterized lick trace. *Bottom*, Mean normalized magnitude of joystick speed and licking aligned to reward delivery (time=0) and reach threshold crossing (time=-1). **c**, Mice adjusted their reach amplitude across the three blocks. Left plot shows data from a single session, right plot shows the data across sessions. **d-f**, Brief closed-loop inactivation of $MCtx^{FL}$ neural activity by driving inhibitory neurons in VGAT-ChR2 mice significantly reduced ongoing reach amplitude (**d**) and speed (**e**), n=3 mice, 2 sessions/mouse. **f**, Open-loop inactivation of $MCtx^{FL}$ triggered around the end of ITI significantly decreased probability of reach initiation. **g**, Recordings were made in $MCtx^{FL}$ and striatum with a Neuropixels probe, which densely sampled neural activity in the depth axis spanning approximately 3.8 mm (n=10 hemispheres, N=6 mice). **h**, Many units exhibited activity correlated with movement kinematics as exemplified by the two $MCtx^{FL}$ units that modulated their firing rates in proportion to movement amplitude. **i**, Task-related neural activity was widely distributed across the depth of recordings. Mean z-score normalized activity at each depth from the pial surface. **j**, A schematic drawing of principal component (PC) and movement-kinematic (**KN**) dimensions found by dimensionality reduction within the population state space where each axis represents the activity of an individual neuron. By projecting neural population activity at every moment in time onto the KN dimension, we obtain 'neural trajectories' capturing co-modulation of neural population activity as a function of movement amplitude. **k**, Cross-validated neural trajectories of movement-amplitude tertiles differed significantly along the KN dimension. **l**, Units whose activity significantly covaried with movement speed were distributed across all cortical layers. Each dot is a single recorded unit. Values are Pearson correlation coefficient and the corresponding p-value for each unit. **m**, Time of peak activity shown by depth. Peak activity time was taken for each row in **i**.

Figure 2. Inhomogeneous laminar distribution of movement-timed activity in $MCtx^{FL}$

a, *Top*, Labelling of pons-projecting PT neurons (green) and the probe tract (red) with light sheet microscopy on a cleared hemibrain (see Extended Data Figs. 2 & 3 for more coronal and sagittal images). Scale bar=1mm. *Bottom*, Probe tracks reconstructed in 3D volume were warped to Allen Anatomical Template (AAT), and each electrode site was annotated using Allen Reference Atlas (ARA). **b**, $MCtx^{FL}$ neural activity projected onto the top three PCs (Methods). PCs were classified as 'Move+', if the neural trajectory on each PC dimension (PC score) peaked before +500 ms relative to the reach start. Other PCs that peaked afterwards with negative modulation during reach were classified as 'Move-'. **c**, *Left*, Weights of move+ PCs are plotted as a function of recording depth across all cortical neurons (solid circles). A dotted line indicates the histologically-verified cortical border (1.75 mm, see Methods and Extended Data Fig. 3). *Right*, Weights of move- PCs are plotted as a function of recording depth. **d**, Weights of move+ and move- PCs significantly differ across cortical depths. **e**, *Left*, Performance of decoding illustrated on 20 repetitions (concatenated, randomized order) of joystick movements that yielded reward. Smoothed x, y position trajectories (1kHz resolution; 300pt 3rd order Savitzky-Golay) are compared with prediction from a consensus linear decoder (see Methods) using 250 simultaneously recorded single units in $MCtx^{FL}$ and striatum. *Center*, Mean ± SEM movement amplitude predicted by the decoder is plotted in blue. The orange trajectory represents the predicted amplitude from a decoder with unit-identity shuffling. *Right*, Boxplot of cross validation decoding performance (Pearson correlation between decoder prediction and observed trajectory) on test subsets for 50 training folds. **f**, Relative contribution of individual units can be informed by their weights comprising the decoder vector. The absolute valued weights were z-score normalized such that a greater value indicates a larger contribution in decoding. The

bioRxiv preprint doi: https://doi.org/10.1101/772517; this version posted January 7, 2021. The copyright holder for this preprint (which was not certified by peer review) is the author/funder, who has granted bioRxiv a license to display the preprint in perpetuity. It is made available under aCC-BY-NC-ND 4.0 International license.

weights are plotted versus the inferred recording depth to reveal the laminar inhomogeneity. Mean ±1SD weights with 1000 laminar position shuffling are also plotted for comparison.

Figure 3. Prevalence of motor command-like activity in IT neurons

a, Normalized mean ± SEM neural activity before and during optical silencing (tagging) of pons-projecting PT^+ neurons. **b**, same as **a** but of striatum-projecting IT^+ neurons. **c**, Change of the mean firing rate of the individual neurons during optical tagging is plotted as a function of the inferred recording depth (x axis). Units with a significant change are plotted with filled circles with the latency of half-maximal firing rate change color-coded. Note that the tagged PT^+ and IT^+ neurons are located in the estimated depths of layer 5 as expected. **d-e**, Raw voltage traces showing spike activity of example PT^+ and IT^+ units with the amplitude of joystick movement superimposed at the top. **f**, *Left*, Trial by trial activity of an example PT^+ neuron to laser (60 trials, 594 nm) during optotagging after completion of task performance. More examples are shown in Extended Data Fig. 7. *Right*, Activity of the same PT^+ neuron aligned to the reach start during task performance. **g**, Z-score normalized activity of all individual PT^+ neurons aligned to the reach start during task performance. **h**, *Left*, Trial by trial activity of an example IT^+ neuron to laser during optotagging. *Right*, Activity of the same IT^+ neuron aligned to the reach start. **i**, Z-score normalized activity of all individual IT^+ neurons aligned to the reach start. **j**, Normalized mean ± SEM activity of PT^+, IT^+ neural populations aligned to reach threshold crossing (ReachT) and reward delivery. The mean activity of the rest (untagged) of $MCtx^{FL}$ is plotted in dotted curves for comparison. **k**, The cumulative distribution of the timing for peak activity is plotted for PT^+ and IT^+ neural populations. Distribution of the rest (untagged) of $MCtx^{FL}$ is plotted in dotted curves for comparison. **l**, The cumulative distribution of the reward to reach activity ratio is plotted for PT^+ and IT^+ neural populations. The ratio greater than 1 means that the corresponding unit displayed a greater response during the reward epoch than the movement epoch of same lengths.

Figure 4. Cell-type specific imaging shows prominent movement-timed activity in IT neurons of superficial layer 5 $MCtx^{FL}$

a, Two-photon calcium imaging was performed from left $MCtx^{FL}$, targeting either layer 5b PT or layer 5a IT neurons (separate experiments). Schematic shows the different brain-wide projection targets of the two cell types. **b**, *Top left*: Histology from 2 imaged mice, one from each of the two mouse lines. Scale bar 100 microns, images are matched for scale. *Top right*: example field of view. *Bottom rows*: Green traces are inferred spike rates of randomly selected IT neurons aligned to behavioral variables below. **c**, Mean normalized activity traces aligned to reach threshold crossing and reward delivery for every unit in the dataset, grouped by projection neuron type. Units are ranked by time of peak activity determined using the unplotted half of trials. Each row normalized to its peak activation. **d**, Top row shows the average normalized joystick speed and lick rate. Bottom row shows mean PT and IT activity. All are aligned to reward delivery. IT neurons show prominent peri-movement activation, whilst PT peak activity occurs later. Units were mean averaged for each projection target, then resulting average was normalized to range 0-1. **e**, Normalized inferred spike rate for individual units with positive or negative PC1 loadings are plotted. Colored dots on the left reflect the cell type. For PCA, PT units were randomly subsampled to match the size of the IT population. Individual principal components, and additional example units, are provided in Extended Data Fig. 8. **f**, Unit weights on the first and second principal components. **g**, Histogram of unit weights on principal component 1 for IT and PT neurons.

Figure 5. $MCtx^{FL}$ IT neurons are necessary for control of forelimb movement kinematics

a, Schematic of closed-loop inactivation paradigm used in the variable amplitude joystick task. **b**, *Left*, Mean ± SEM reach amplitude of unperturbed (green) and IT inactivation (orange) trials. *Right*, Mean reach amplitude of unperturbed and IT inactivation trials broken out for individual sessions (7) and mice (5). **c**, *Left*, Mean ± SEM reach speed of unperturbed (blue) and PT inactivation (orange)

bioRxiv preprint doi: https://doi.org/10.1101/772517; this version posted January 7, 2021. The copyright holder for this preprint (which was not certified by peer review) is the author/funder, who has granted bioRxiv a license to display the preprint in perpetuity. It is made available under aCC-BY-NC-ND 4.0 International license.

trials. *Right*, Mean reach speed of unperturbed and IT inactivation trials for individual sessions. **d**, *Left*, Mean ± SEM reach amplitude of unperturbed (green) and PT inactivation (orange) trials. *Right*, Mean reach amplitude of unperturbed and PT inactivation trials broken out for individual sessions (6) and mice (3). **e**, *Left*, Mean ± SEM reach speed of unperturbed (blue) and PT inactivation (orange) trials. *Right*, Mean reach speed of unperturbed and PT inactivation trials for individual sessions.

Figure 6. Cell-type specific individual neuronal correlation with- and neural population decoding of movement kinematics

a, Individual PT^+ units are plotted based on their normalized movement-timed activity along X axis and their activity modulation as a function of movement amplitude along Y axis (regression coefficients, β). For instance, a unit in the first quadrant is the one that increased its firing rate during movement with a positive correlation with the movement amplitude. Blue-filled circles represent PT^+ units with a significant regression coefficient (*t* test, α=0.05). Gray circles represent the rest of $MCtx^{FL}$ units. Fisher's exact test against a uniform distribution of PT^+ units across quadrants, p=0.84). **b**, same as **a** for individual IT^+ units (Fisher's exact test, p=0.0056). Green-filled circles represent IT^+ units with a significant regression coefficient. **c**, Squared Pearson correlation between normalized firing rate and reach amplitude are plotted for individual PT^+ and IT^+ units color-coded by their mean movement-timed activity. **d**, To gauge how informative the PT^+ neuronal population activity of the movement kinematics relative to other subpopulations, contributions to decoder performance of the separate neural populations either identified by optotagging (PT^+) or inferred from anatomical position (see Methods) are plotted. **e**, Naive Bayes classifiers were trained with cross validation to predict movement amplitude tertile of a given unlabeled trial using all units or separate populations of units either identified by optotagging (PT^+, IT^+) or inferred from anatomical position.

Figure 7. Inactivation of PT and IT neurons oppositely affect striatal activity

a, 3D visualization of complete single neuron reconstructions [2] from the PT (top) and IT (bottom) anatomical classes, illustrating integration of PT and IT neuronal projections in striatum. **b**, Change in the PT^+ neuronal activity due to the movement-triggered inactivation during task performance. **c**, Change in the IT^+ neuronal activity due to the movement-triggered inactivation during task performance. **d**, Change in the downstream striatal activity during PT or IT neuronal inactivation illustrates opposite effects. **e**, The effect of PT inactivation on the firing rate of putative medium spiny neurons (left) and putative interneurons (right). **f**, *Left*, The mean 2D joystick trajectory of PT inactivation versus control trials from an example session, illustrating the lateral deviation (X axis) due to PT inactivation. *Center*, The mean ± SEM joystick X trajectory is plotted for all PT inactivation sessions. *Right*, The mean ± SEM joystick X trajectory is plotted for all IT inactivation sessions. **g**, *Left*, dSTR neural population activities of all sessions are projected to the KN dimension and plotted separately for movement amplitude tertiles. *Center*, PT inactivation did not lead to a significant change in the $KN^{dim.}$. *Right*, IT inactivation led to a significant decrease in the $KN^{dim.}$ projection score.

Extended Data Figure 1. Stimulation of layer 5 output neurons in $MCtx^{FL}$ invigorates forelimb movement

Closed loop stimulation of the majority of descending layer 5 output neurons in $MCtx^{FL}$ labelled using the Rbp4-cre line [53,89] crossed to Ai32[77] produced increases in the amplitude (*top*) and speed (*bottom*) of forelimb movement.

Extended Data Figure 2. Histological verification of PT and IT neuronal labelling

a, Expression of fluorescently-labelled FLInChR in the deep layer 5 PT neurons of Sim1-cre mice. **b**, Fluorescent labelling of the medullary pyramid in PT mice. **c**, Expression of FLInChR in the layer 5 IT neurons of Tlx3-cre mice. **c**, To compare the laminar distribution of PT and IT neurons in the motor cortex, the intensity of fluorescence was measured along a line oriented from the pial surface through M1 to the dorsal surface of STR. This distance was normalized to 1800 microns which is our

bioRxiv preprint doi: https://doi.org/10.1101/772517; this version posted January 7, 2021. The copyright holder for this preprint (which was not certified by peer review) is the author/funder, who has granted bioRxiv a license to display the preprint in perpetuity. It is made available under aCC-BY-NC-ND 4.0 International license.

estimate from the allen mouse brain atlas. The fluorescence intensity data were binned into 250 evenly spaced bins and averaged within each bin. The binned data were normalized to max intensity for each cell type.

Extended Data Figure 3. Histological and physiological estimation of the cortex border

a, A sagittal (top) and coronal (bottom) view of a cleared mouse hemi brain imaged with light sheet microscopy. Green fluorescence indicates labeling of the deep layer 5 PT neurons and their projections to downstream areas such as striatum, superior colliculus and pons. Red fluorescence indicates probe tracks. Numbers in the top and bottom rows indicate medial-lateral and anterior-posterior coordinates relative to bregma, respectively. The length of the white scale bar = 1mm. **b**, Three dimensional rendering of probe tracks with the Allen Anatomical Template (AAT). Imaged 3D brain volumes were aligned to AAT, and each electrode on Neuropixels probe was assigned to a brain region using the probe geometry and Allen Reference Atlas (Methods). All cells recorded from electrodes located at the pial depth of 1.75 mm or upper (estimated by the manipulator) were assigned a motor cortical region. **c**, Estimated root mean square voltage (RMS) is plotted versus the pial depth. Note the trough indicating dearth of neural activity around the depth of 1.75 mm, which is consistent with the histologically estimated cortical border. **d**, Mean event rate is plotted versus the pial depth. An event is defined as voltage crossing (e.g. spikes) a threshold (80 μV). Note the elevated event rates of the cortical depths. **e**, Threshold-crossing events are binned and counted based on the absolute raw amplitude for each pial depth. **f**, Mean event rates are plotted for each electrode site tiling the Neuropixel probe. Note the higher event rates within the cortical range as well as the dearth of events around the histologically estimated cortical border (1.75 mm). RMS and event rates were measured using codes written by Jennifer Colonell (https://github.com/jenniferColonell/Neuropixels_evaluation_tools).

Extended Data Figure 4. Summary of cortical and striatal neural population activity during task performance

a, Mean z-score normalized activity aligned to reach threshold crossing and reward delivery (x axis) is plotted per inferred depth (y axis) relative to the pial surface for all individual recording sessions (N=10). **b**, $MCtx^{FL}$ neural population activity of movement amplitude tertiles are projected onto the top three principal components. Neural trajectories indicate that at least partially separable populations of neurons are active during forelimb movements scaling with reach amplitude. Other populations appear to be active during reward collection.

Extended Data Figure 5. Projection of striatal neural population activity onto top three PCs

Striatal neural population activity of movement amplitude tertiles are projected onto the top three principal components. Similar to the cortical data, neural trajectories indicate that at least partially separable populations of neurons are active during forelimb movements or reward collection.

Extended Data Figure 6. Projection of $MCtx^{FL}$ population activity onto the cross-validated KN dimension

Each panel represents $MCtx^{FL}$ data from each recording session. In each iteration, half of the trials were randomly selected and used to define the $KN^{dim.}$, along which the variance of neural population activity was best explained by variance in forelimb movement amplitude. Data from the other half of the trials were projected to the $KN^{dim.}$ (2-fold cross validation). Total 1000 iterations were run for data from each session, results of randomly selected 100 trials are plotted for simplicity.

Extended Data Figure 7. PT^{+} and IT^{+} neuronal activity during task performance and optotagging

Blue-colored rasters in the left column illustrate trial by trial individual neuronal responses during

bioRxiv preprint doi: https://doi.org/10.1101/772517; this version posted January 7, 2021. The copyright holder for this preprint (which was not certified by peer review) is the author/funder, who has granted bioRxiv a license to display the preprint in perpetuity. It is made available under aCC-BY-NC-ND 4.0 International license.

task performance (left panel of each pair, aligned to reach start) with significant inhibitory responses during optotagging (right panel of each pair, aligned to laser onset) in Sim1-Cre (KJ18Gsat) mice injected with rAAV2-retro-CAG-Flex-FLInChR-mVenus to the pons. Each row represents each trial. The mean ± SEM spike rate (Hz) is superimposed. Numbers on the left and right ordinates of each plot indicate the number of trial and firing rate in Hz, respectively. Green-colored rasters in the right column illustrate trial by trial IT^+ individual neuronal responses during task performance (left panels) and optotagging (right panels) in Tlx3-Cre (PL56Gsat) mice.

Extended Data Figure 8. Further information about spike deconvolution from calcium imaging data and PCA with the inferred spike rate data.

a, Illustration of spike deconvolution. Panel shows 5 example regions of interest, each of two rows. Top row for each unit (blue) shows the dF/F trace, with the row beneath (red) showing the inferred spike activity metric. **b**, a zoomed-in portion for three units from **a**. **c**, Structure of first four principal components of neural activity across all units in the dataset, aligned to reward. **d**, The fraction of explained variance for the top 10 principal components in the dataset. **e**, *left*, The normalized inferred spike rates of representative units with most positive (top 100 rows) and negative (bottom 100 rows) weights for PC1 are plotted. Format same as Figure 3e. *right*, The normalized inferred spike rates of representative units with positive (top 100 rows) and negative (bottom 100 rows) weights for PC2 are plotted.

Extended Data Figure 9. Robust PT^+ and IT^+ neuron inactivation during task performance

a, An example PT^+ neuron displays a robust inactivation by the laser triggered at the earliest detection of reach in randomly selected trials (top raster rows; bottom raster rows represent control trials). The mean ± SEM spike density (Hz) functions are superimposed for laser and control trials. **b**, Change of all individual PT^+ neuronal activity by opto-silencing aligned to the movement onset. **c**, An example IT^+ neuron displays a robust inactivation by the laser. **d**, Change of all individual IT^+ neuronal activity by opto-silencing.

Extended Data Figure 10. Individual dSTR neuronal responses during task performance and optotagging

Rasters in the left column illustrate trial by trial individual neuronal responses during task performance (left panel of each pair, aligned to reach start) and optotagging (right panel of each pair, aligned to laser onset) in Sim1-Cre (KJ18Gsat) mice injected with rAAV2-retro-CAG-Flex-FLInChR-mVenus to the pons. Format same as Extended Data Fig. 6.

bioRxiv preprint doi: https://doi.org/10.1101/772517; this version posted January 7, 2021. The copyright holder for this preprint (which was not certified by peer review) is the author/funder, who has granted bioRxiv a license to display the preprint in perpetuity. It is made available under aCC-BY-NC-ND 4.0 International license.

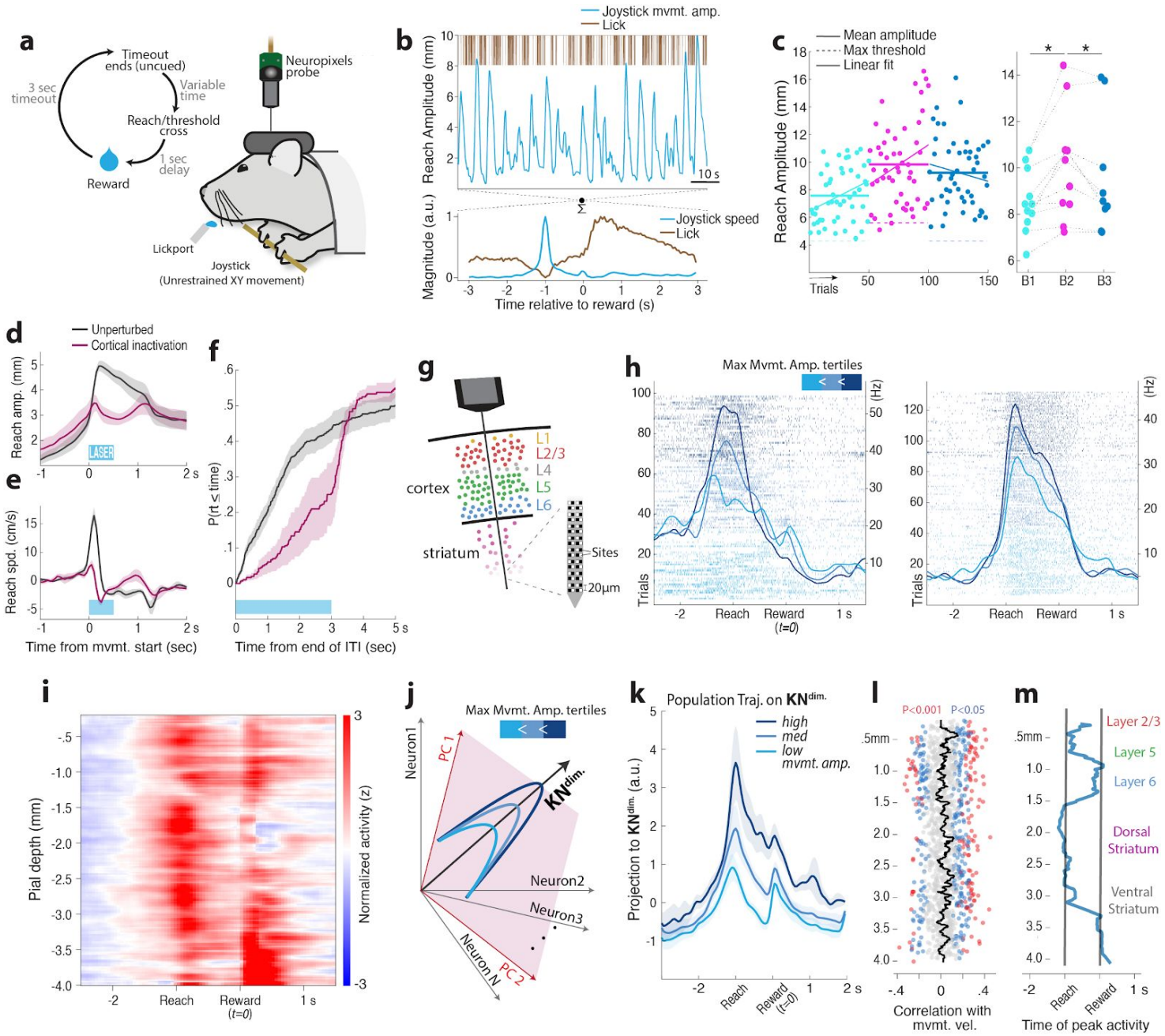

Figure 1

bioRxiv preprint doi: https://doi.org/10.1101/772517; this version posted January 7, 2021. The copyright holder for this preprint (which was not certified by peer review) is the author/funder, who has granted bioRxiv a license to display the preprint in perpetuity. It is made available under aCC-BY-NC-ND 4.0 International license.

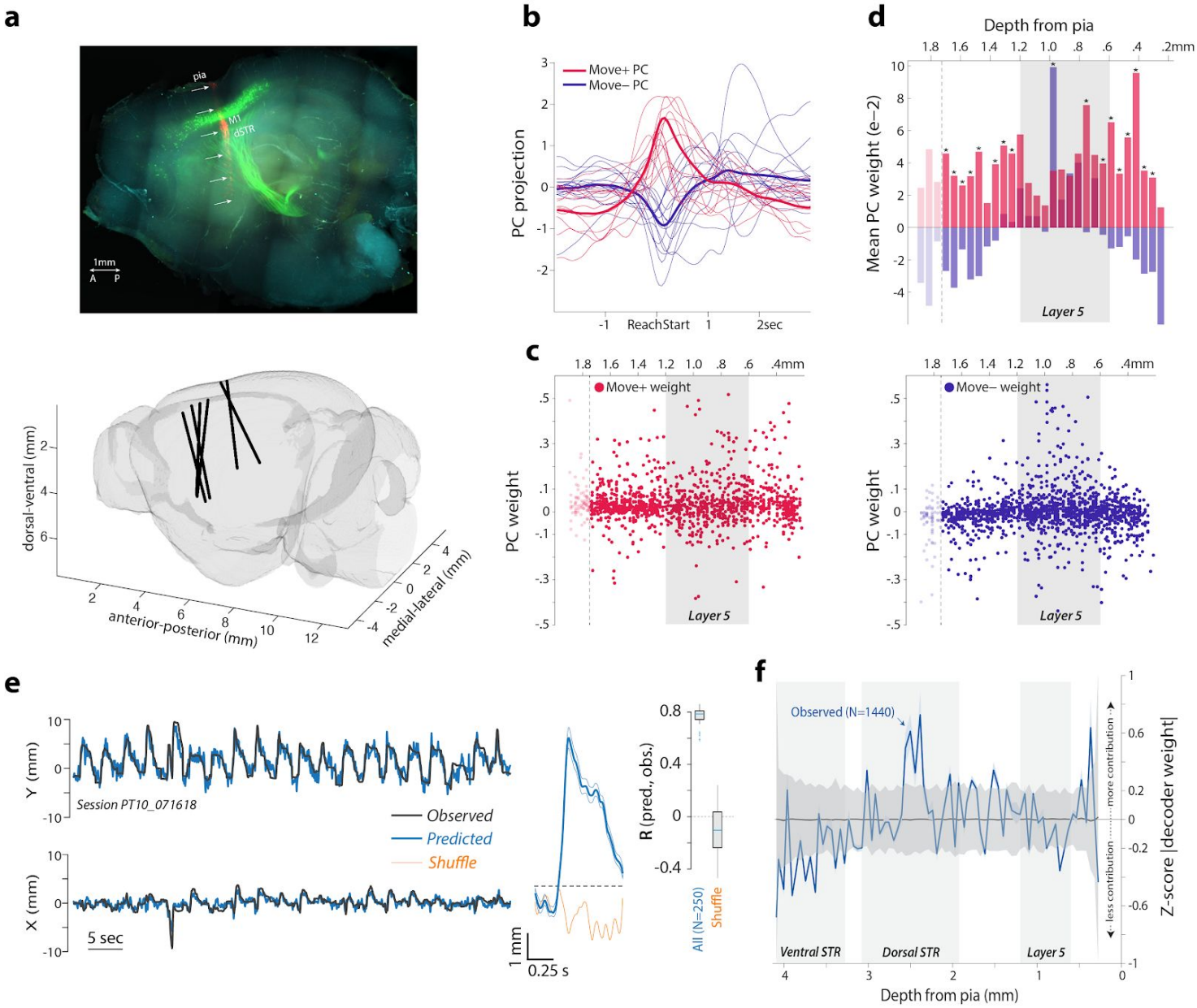

Figure 2

bioRxiv preprint doi: https://doi.org/10.1101/772517; this version posted January 7, 2021. The copyright holder for this preprint (which was not certified by peer review) is the author/funder, who has granted bioRxiv a license to display the preprint in perpetuity. It is made available under aCC-BY-NC-ND 4.0 International license.

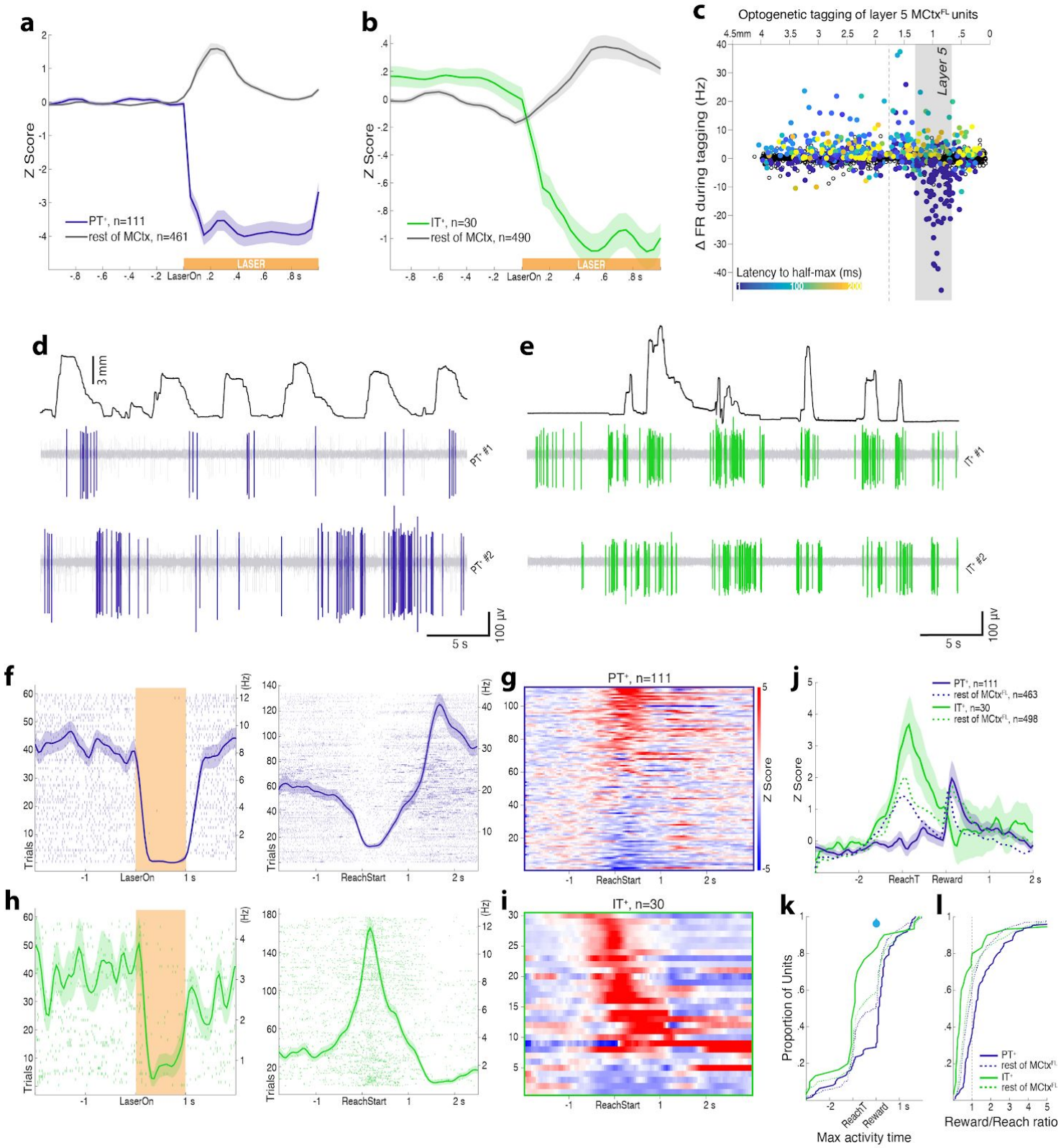

Figure 3

bioRxiv preprint doi: https://doi.org/10.1101/772517; this version posted January 7, 2021. The copyright holder for this preprint (which was not certified by peer review) is the author/funder, who has granted bioRxiv a license to display the preprint in perpetuity. It is made available under aCC-BY-NC-ND 4.0 International license.

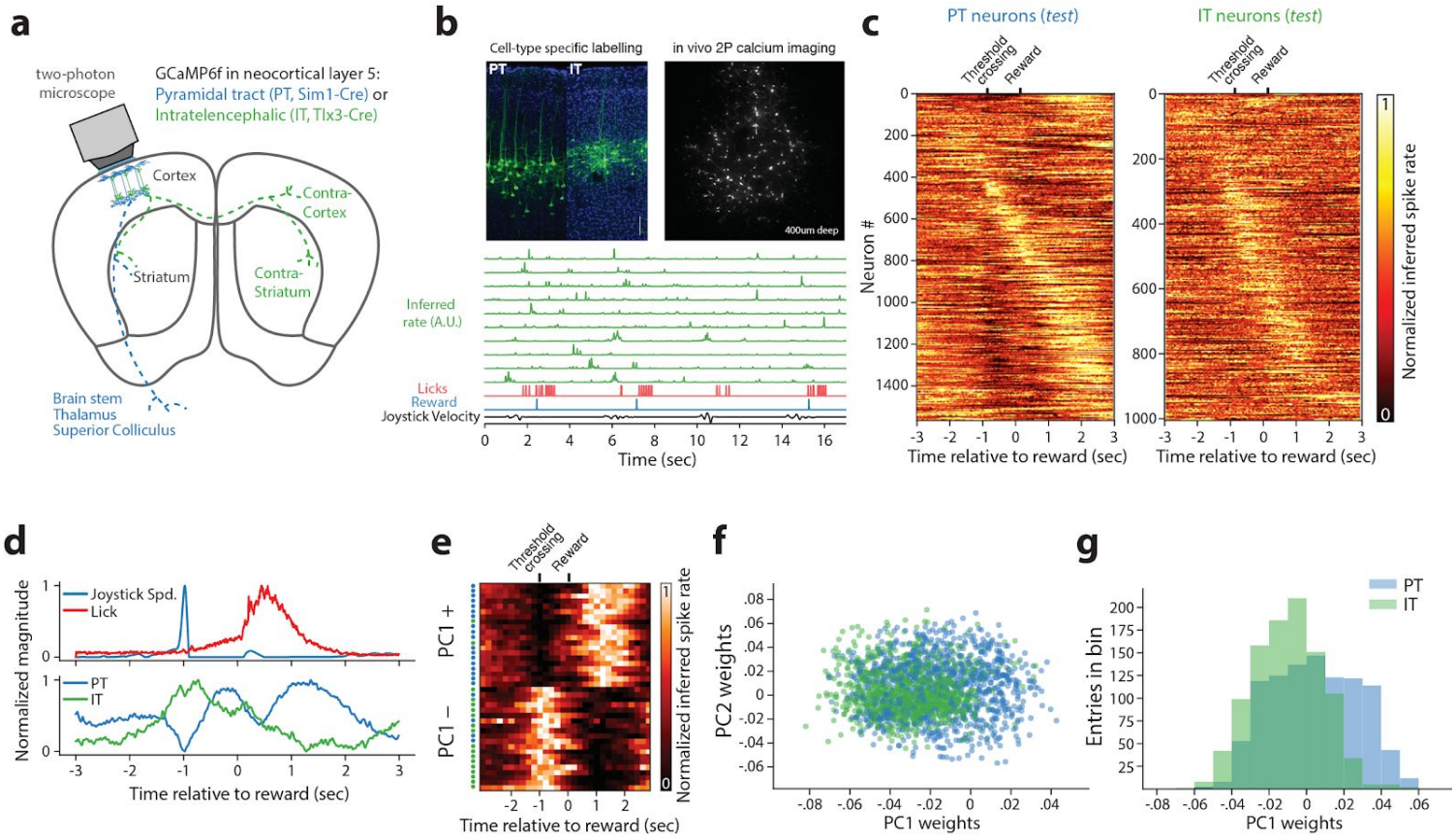

Figure 4

bioRxiv preprint doi: https://doi.org/10.1101/772517; this version posted January 7, 2021. The copyright holder for this preprint (which was not certified by peer review) is the author/funder, who has granted bioRxiv a license to display the preprint in perpetuity. It is made available under aCC-BY-NC-ND 4.0 International license.

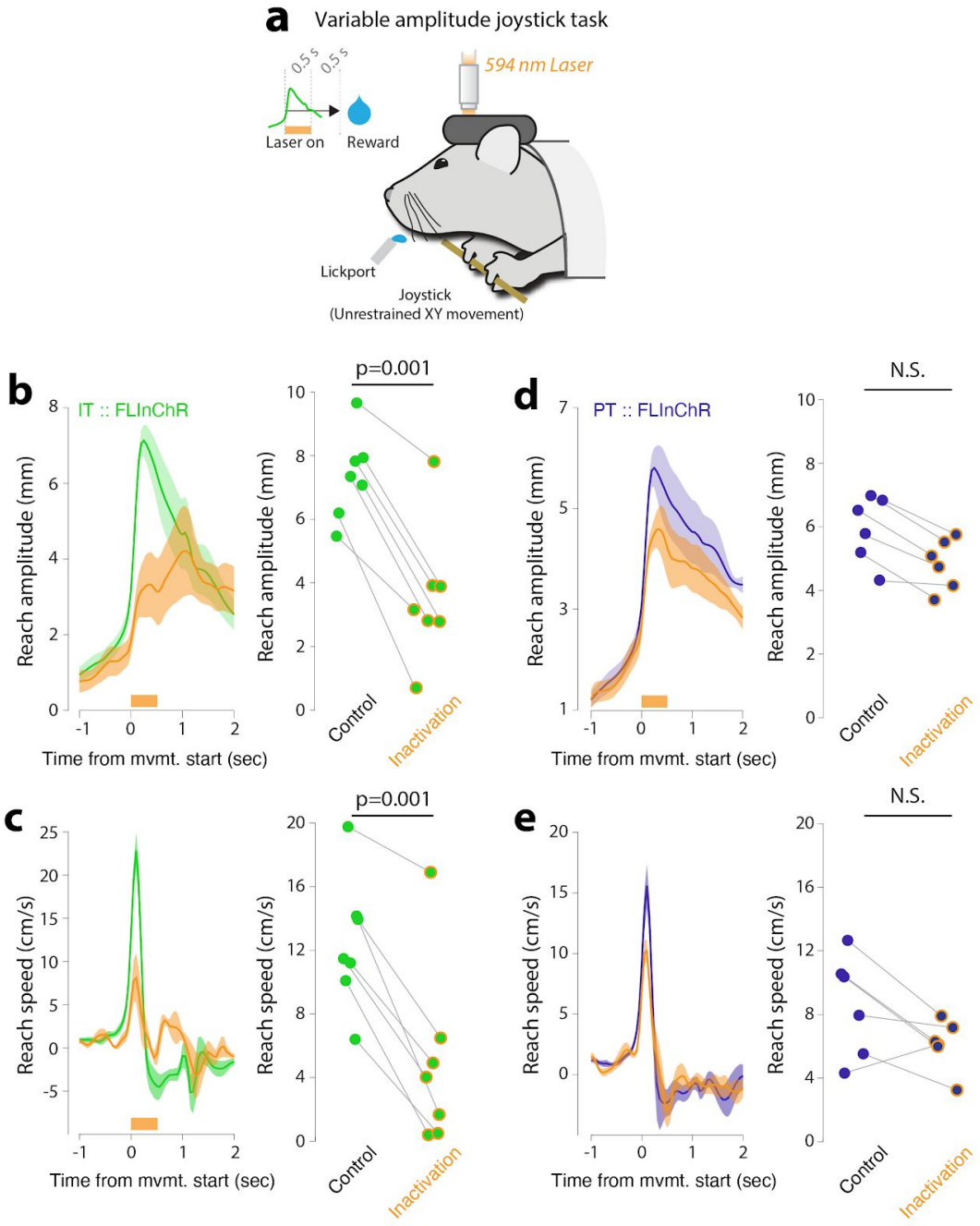

Figure 5

bioRxiv preprint doi: https://doi.org/10.1101/772517; this version posted January 7, 2021. The copyright holder for this preprint (which was not certified by peer review) is the author/funder, who has granted bioRxiv a license to display the preprint in perpetuity. It is made available under aCC-BY-NC-ND 4.0 International license.

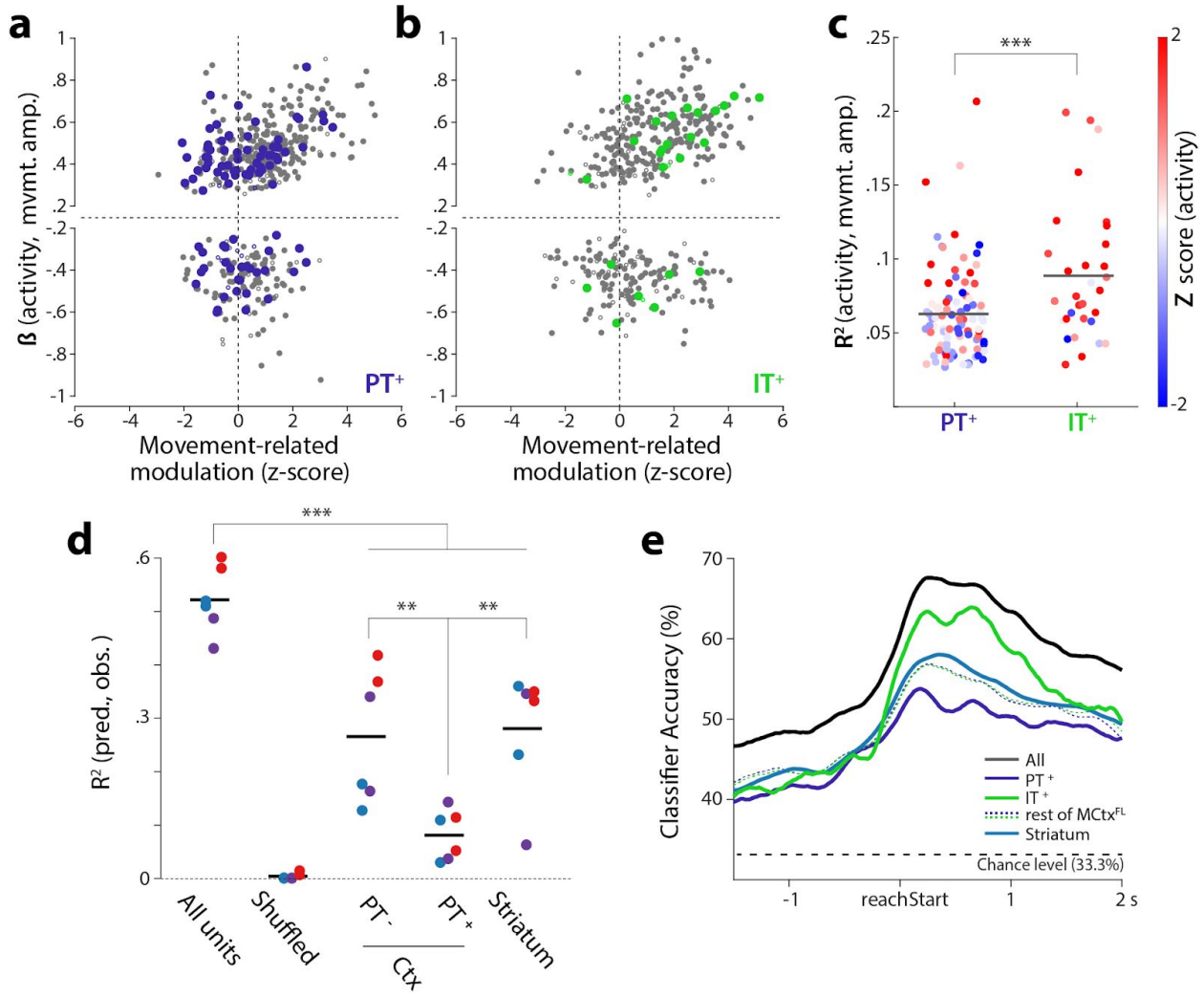

Figure 6

bioRxiv preprint doi: https://doi.org/10.1101/772517; this version posted January 7, 2021. The copyright holder for this preprint (which was not certified by peer review) is the author/funder, who has granted bioRxiv a license to display the preprint in perpetuity. It is made available under aCC-BY-NC-ND 4.0 International license.

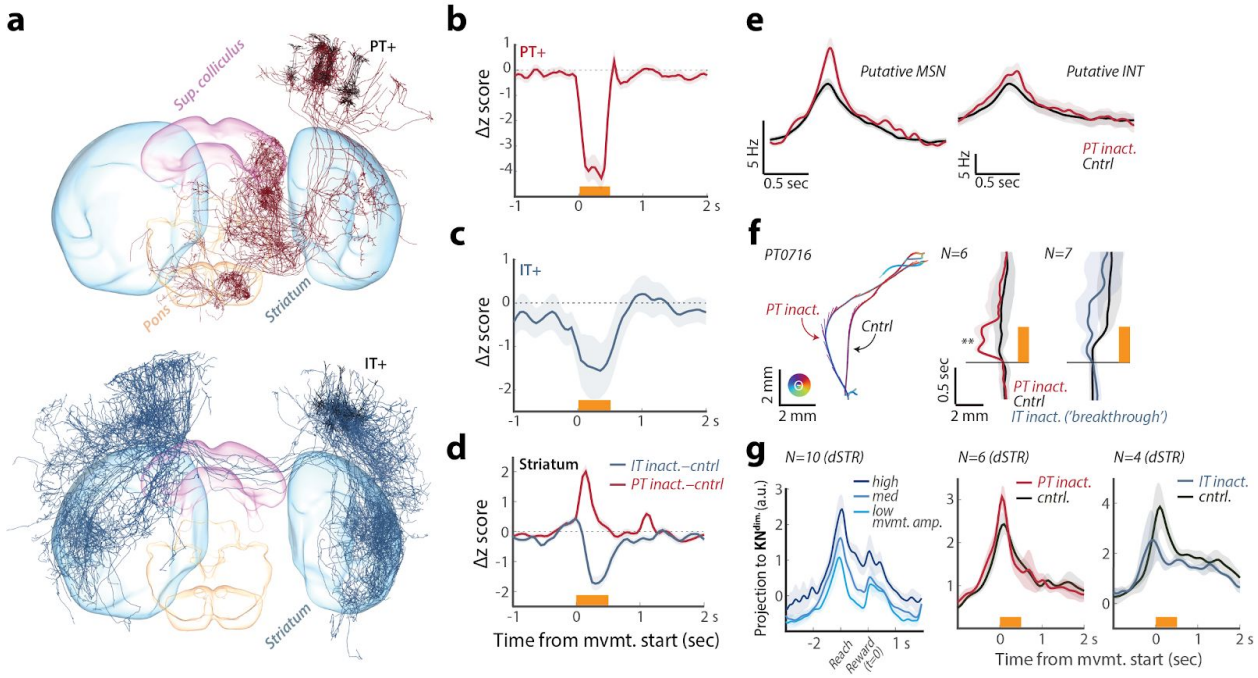

Figure 7

bioRxiv preprint doi: https://doi.org/10.1101/772517; this version posted January 7, 2021. The copyright holder for this preprint (which was not certified by peer review) is the author/funder, who has granted bioRxiv a license to display the preprint in perpetuity. It is made available under aCC-BY-NC-ND 4.0 International license.

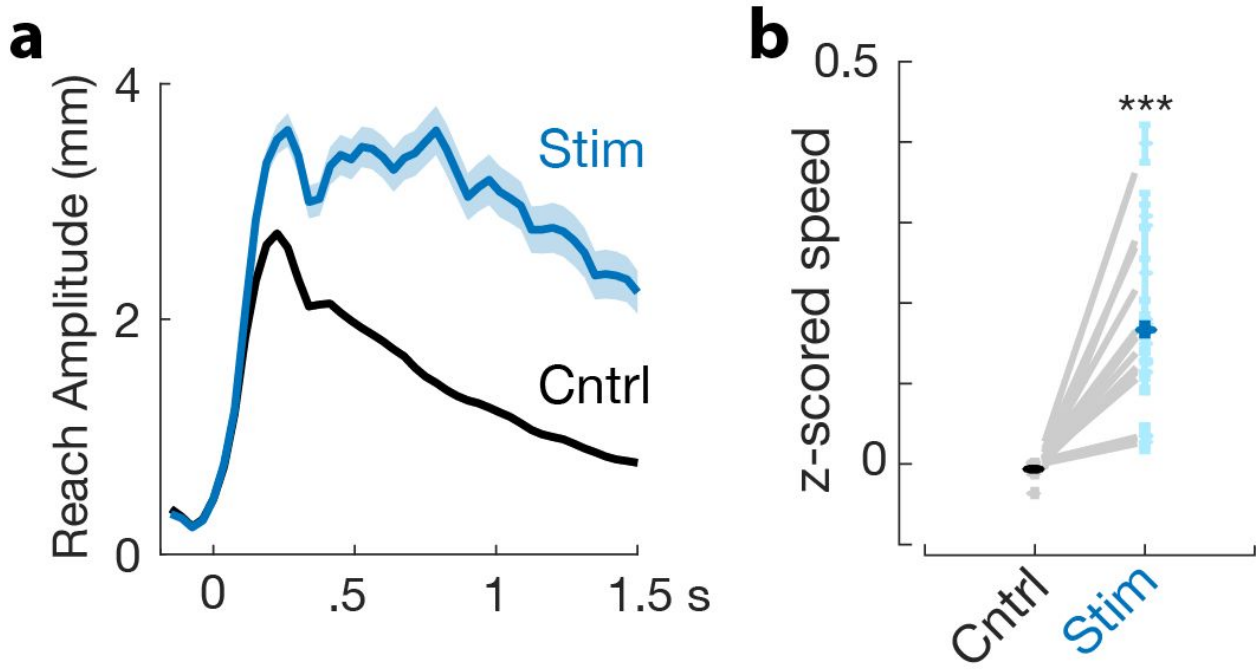

Extended Data Fig. 1

bioRxiv preprint doi: https://doi.org/10.1101/772517; this version posted January 7, 2021. The copyright holder for this preprint (which was not certified by peer review) is the author/funder, who has granted bioRxiv a license to display the preprint in perpetuity. It is made available under aCC-BY-NC-ND 4.0 International license.

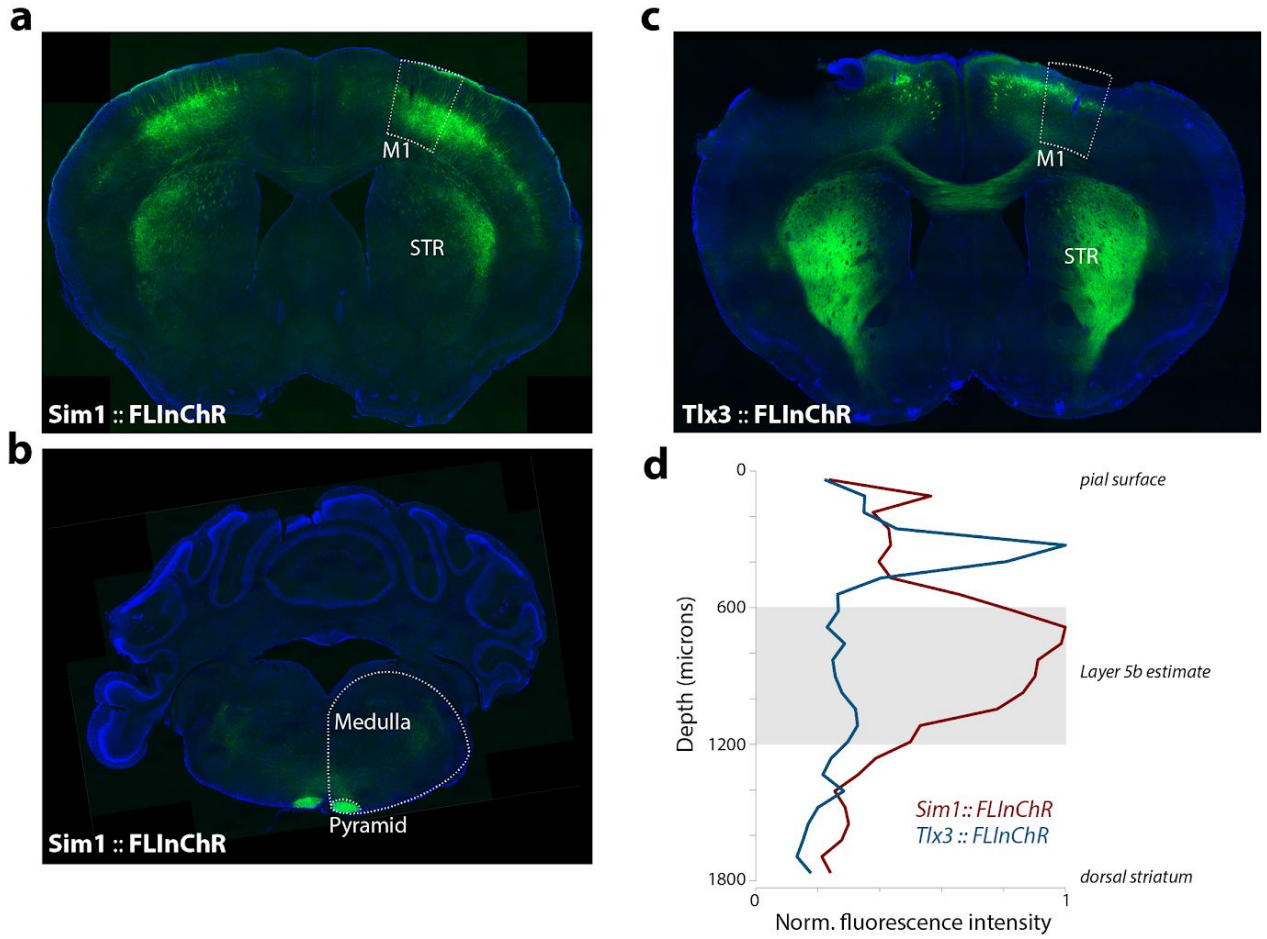

Extended Data Fig. 2

bioRxiv preprint doi: https://doi.org/10.1101/772517; this version posted January 7, 2021. The copyright holder for this preprint (which was not certified by peer review) is the author/funder, who has granted bioRxiv a license to display the preprint in perpetuity. It is made available under aCC-BY-NC-ND 4.0 International license.

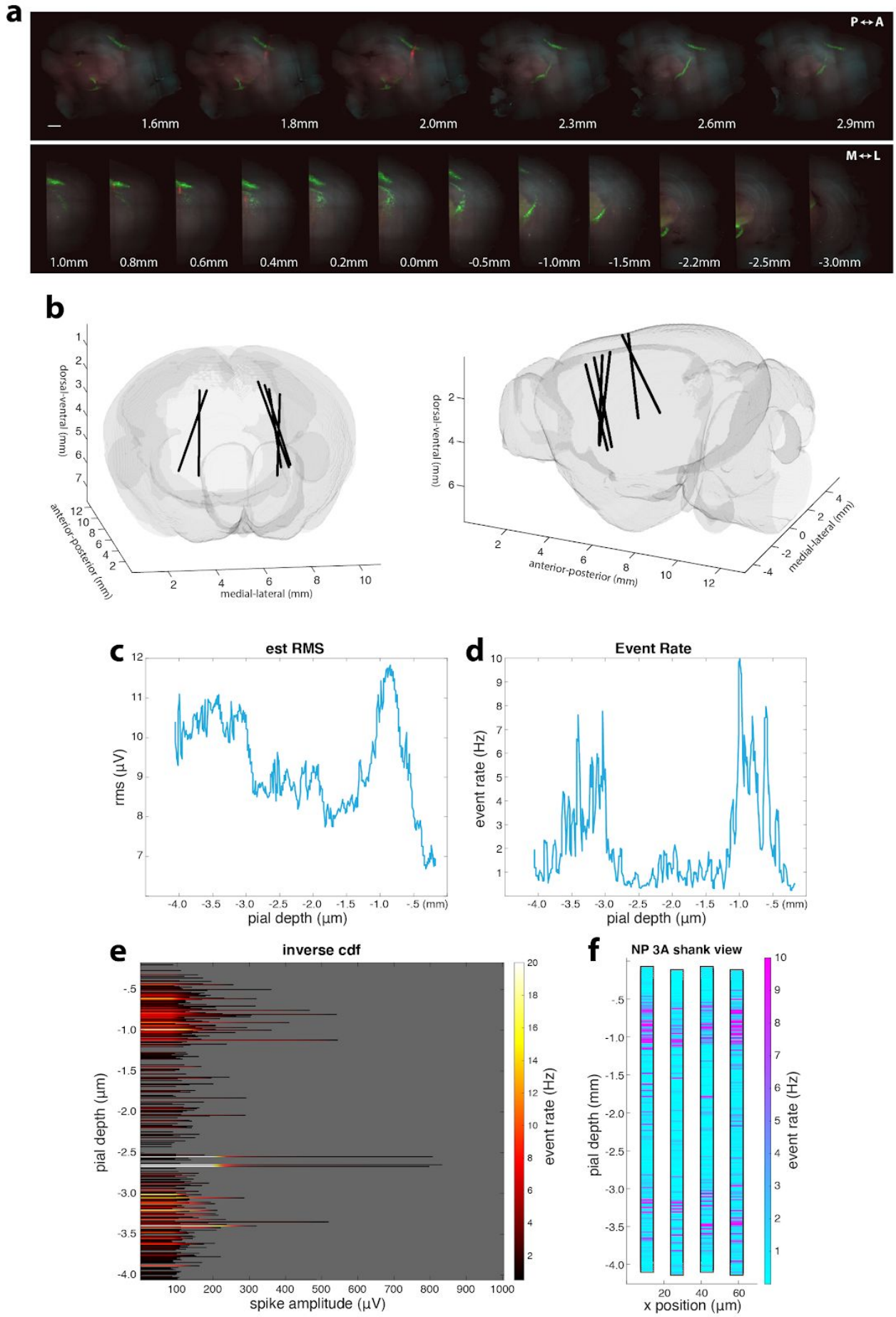

bioRxiv preprint doi: https://doi.org/10.1101/772517; this version posted January 7, 2021. The copyright holder for this preprint (which was not certified by peer review) is the author/funder, who has granted bioRxiv a license to display the preprint in perpetuity. It is made available under aCC-BY-NC-ND 4.0 International license.

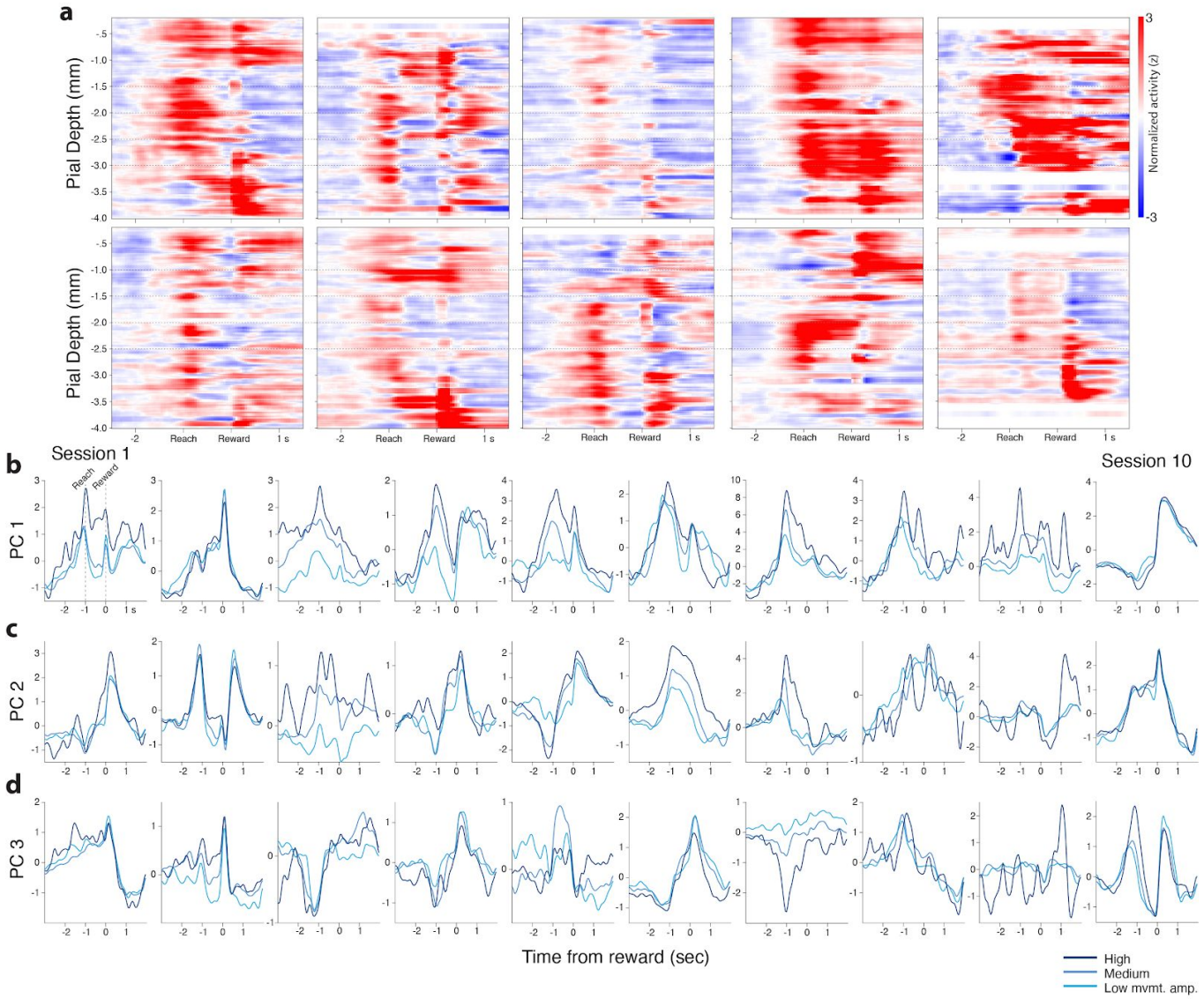

Extended Data Fig. 4

bioRxiv preprint doi: https://doi.org/10.1101/772517; this version posted January 7, 2021. The copyright holder for this preprint (which was not certified by peer review) is the author/funder, who has granted bioRxiv a license to display the preprint in perpetuity. It is made available under aCC-BY-NC-ND 4.0 International license.

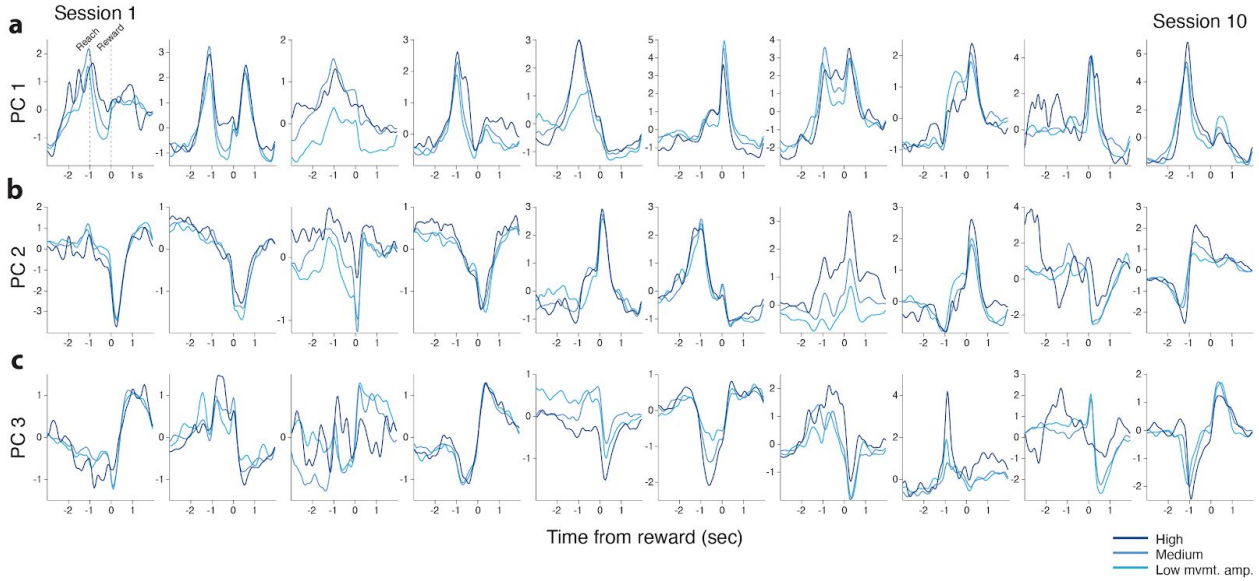

Extended Data Fig. 5

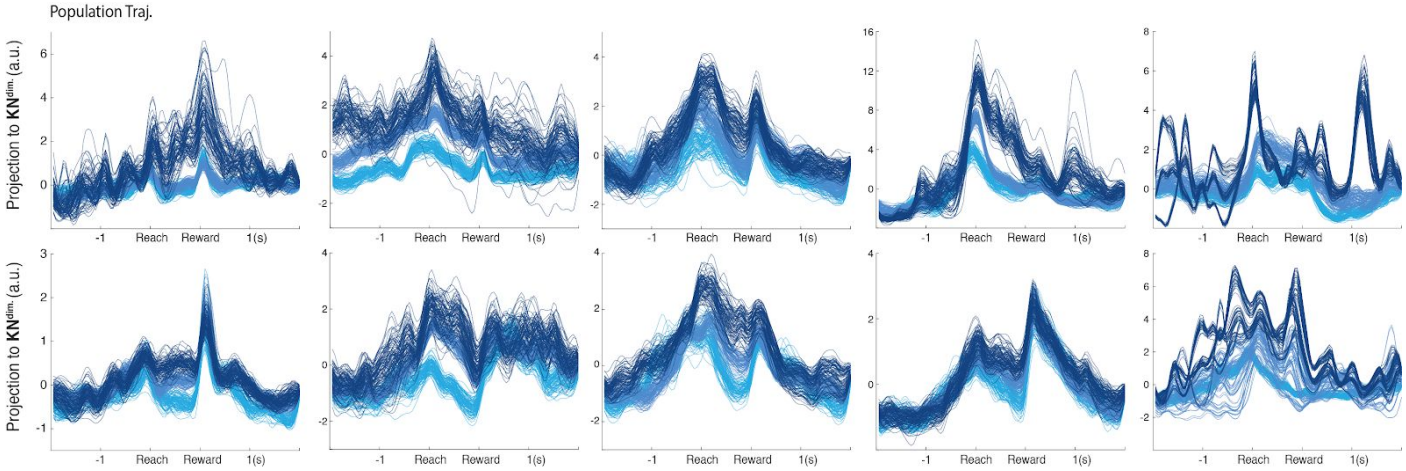

Extended Data Fig. 6

bioRxiv preprint doi: https://doi.org/10.1101/772517; this version posted January 7, 2021. The copyright holder for this preprint (which was not certified by peer review) is the author/funder, who has granted bioRxiv a license to display the preprint in perpetuity. It is made available under aCC-BY-NC-ND 4.0 International license.

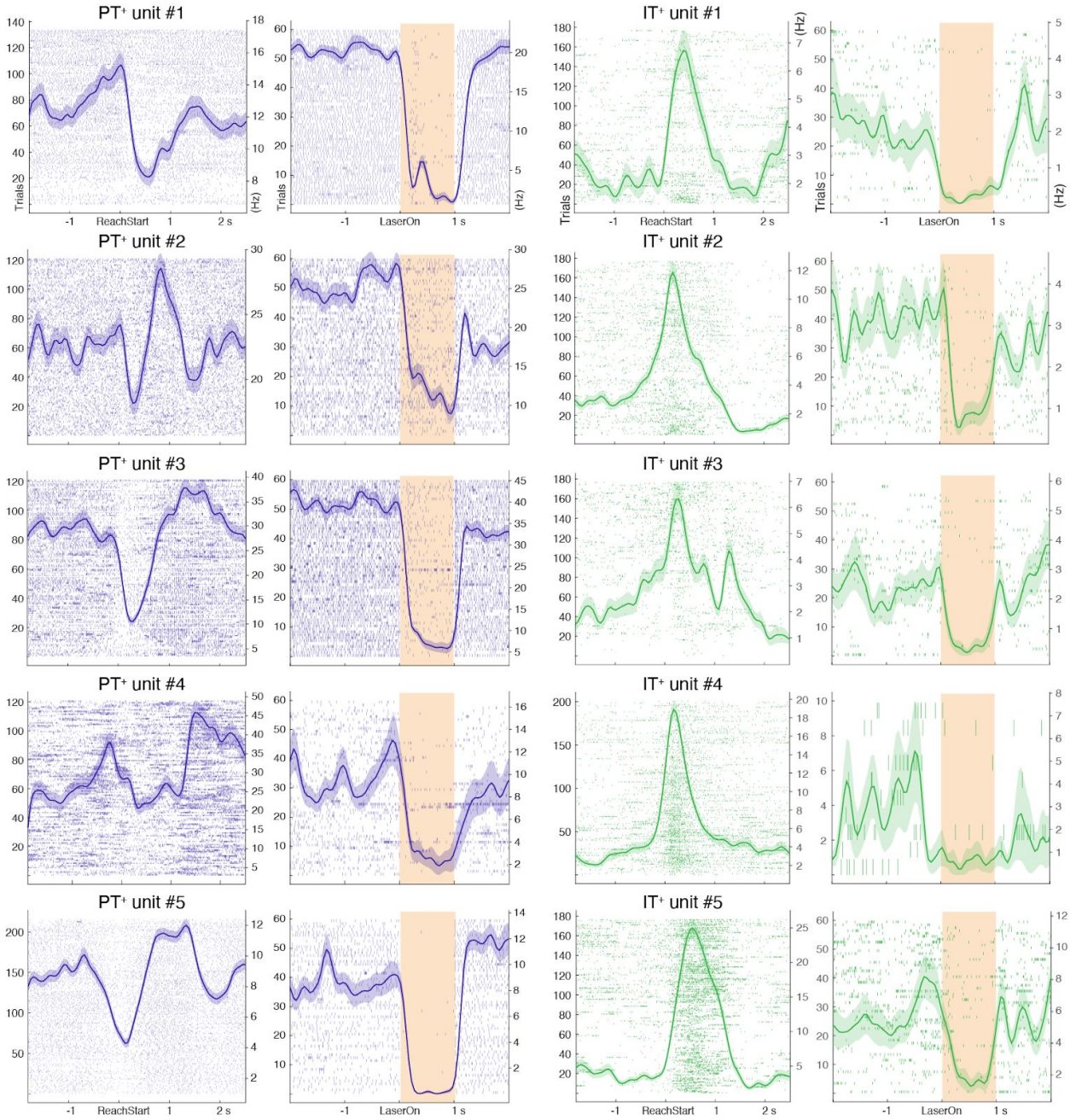

Extended Data Fig. 7

bioRxiv preprint doi: https://doi.org/10.1101/772517; this version posted January 7, 2021. The copyright holder for this preprint (which was not certified by peer review) is the author/funder, who has granted bioRxiv a license to display the preprint in perpetuity. It is made available under aCC-BY-NC-ND 4.0 International license.

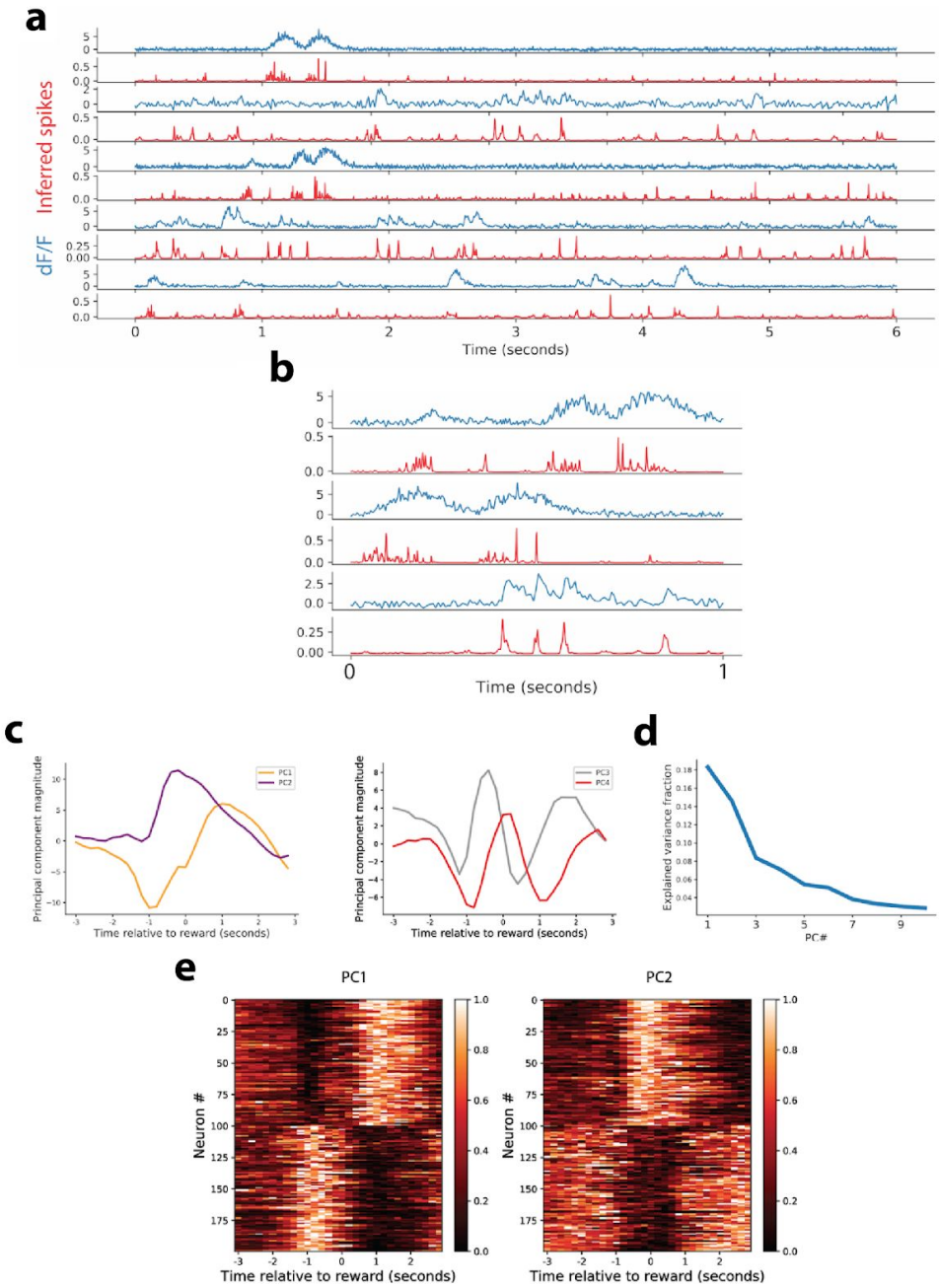

Extended Data Fig. 8

bioRxiv preprint doi: https://doi.org/10.1101/772517; this version posted January 7, 2021. The copyright holder for this preprint (which was not certified by peer review) is the author/funder, who has granted bioRxiv a license to display the preprint in perpetuity. It is made available under aCC-BY-NC-ND 4.0 International license.

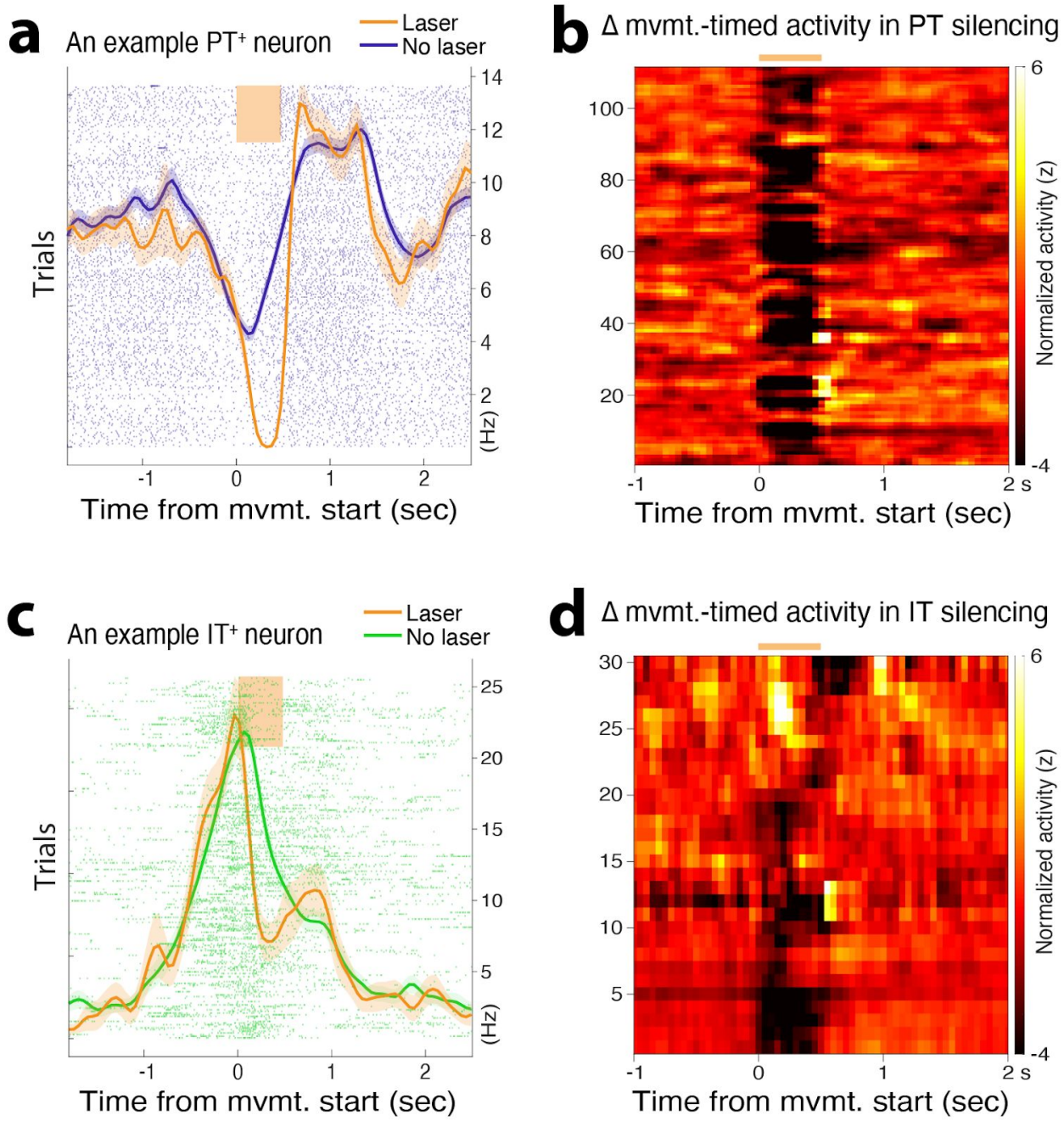

Extended Data Fig. 9

bioRxiv preprint doi: https://doi.org/10.1101/772517; this version posted January 7, 2021. The copyright holder for this preprint (which was not certified by peer review) is the author/funder, who has granted bioRxiv a license to display the preprint in perpetuity. It is made available under aCC-BY-NC-ND 4.0 International license.

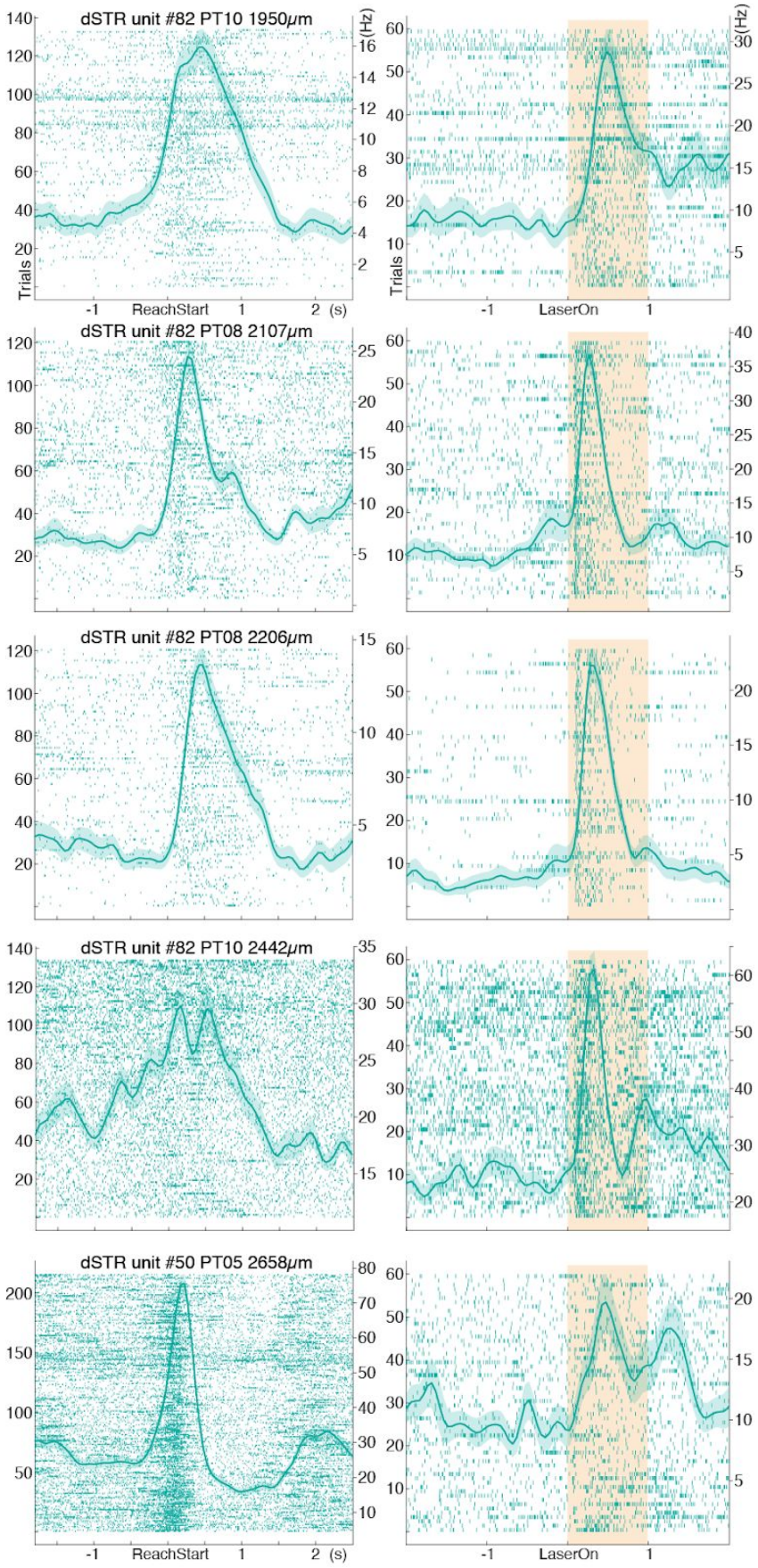

Extended Data Fig. 10